View metadata, citation and similar papers at core.ac.uk
brought to you by CORE
provided by CERN Document Server

Measurement of Electroweak Effects in Small Angle Bhabha Scattering with the DELPHI Detector at LEP

by

Sindre Rødseth Hansen

A thesis submitted to the
Faculty of the Department of Physics of the
University of Oslo in partial fulfillment
of the requirements for the degree
Cand. Scient.
March 1996

Abstract

Two methods are used to measure weak contributions to the Bhabha cross section in the acceptance of the DELPHI Small Angle Tagger. Data taken with the Small Angle Tagger and the Very Small Angle Tagger in 1993 are used. Theoretical formulae of the cross section in the above acceptance containing leading higher-order weak corrections are implemented in a computer program, and a study of various weak contributions has been performed. Corrections to the number of light neutrino species in Nature due to the introduction of weak higher-order corrections in the SAT visible cross section in the luminosity measurement, are determined.

Acknowledgments

I would like to thank my thesis advisor, Alex Read, for his help and support during the work of this thesis. I also thank him for reading through my thesis, making comments and correcting my English. In addition, I thank the rest of the people in the High Energy Physics Group in Oslo. A special thank goes to Trond Myklebust for solving all problems I have encountered with the VAX-VMS and UNIX systems, and for help on getting my own Linux system at home up and running. I would also like to thank my fellow students Esben Lund, Vidar Lund and Bernt Olav Rostad for help on all kinds of difficulties.

Contents

Chapter 1

Introduction

One of man's enduring hopes has been to find a few simple general laws that would explain why Nature with all its seeming complexity and variety is the way it is. Today the closest we can get to an unified view of Nature is a description of the "fundamental" constituents of matter; the elementary particles, and their mutual interactions. In the last forty years there has been dramatic progress in our understanding of these particles and the forces between them. This has resulted in the formulation of the Standard Model of particle physics, which seems to provide, at least in principle, a microscopic basis for all known physical phenomena except gravity.

The Standard Model attempts to explain all the phenomena of particle physics in terms of the properties and interactions of a small number of particles of three distinct types: the spin 1/2 fermions *leptons* and *quarks* and the spin-1 *gauge bosons*.

One of the forces acting between these fermions is the weak force, where nuclear β-decay, which was observed already at the end of the last century, is the most famous example of an interaction with such a force acting. Fermi postulated in 1935 a pointlike interaction between four fermions to describe β-decay, of strength G [1],

$$G \equiv \frac{g^2}{M_P^2} \simeq 10^{-5} GeV^{-2}, \tag{1.1}$$

where M_P is the mass of the massive propagator P, and the weak couplings to the quarks and leptons are denoted by the single number g. Later in this century, processes such as the $\pi - \mu$ and $\mu - e$ decays were discovered and were found to have lifetimes in the region of the β-decay lifetime. The concept of a distinctive class of interactions began to emerge and in the 1950's the discovery of parity non-conservation in β-decays led to the formation of the V$-$A theory of electroweak interactions. This V$-$A (vector-axial vector) structure of the weak currents emerged from the experimental fact that only left handed fermions are present in the weak interactions. This theory however turned out to have prob-

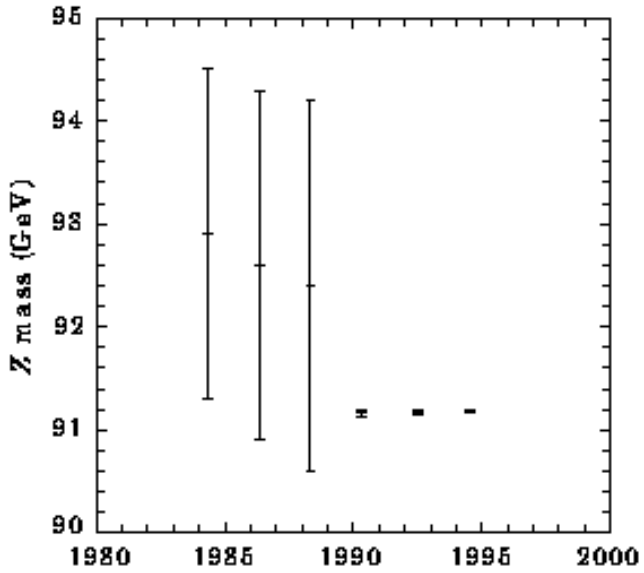

Figure 1.1: The Z^0 mass together with its uncertainty as a function of the years from 1980-1995 [5]. The dramatic improvement in the uncertainty after 1989 comes from the fact that the LEP accelerator became operative.

lems with renormalisability[1]. The introduction of massive gauge bosons and a spontaneous broken gauge theory, in which the gauge boson masses were generated by the Higgs mechanism, resolved this problem, and formed a theory known as the Glashow-Salam-Weinberg theory. This theory, also known as the Standard Model of electroweak interactions, unified the weak and electromagnetic forces, and also predicted the existence of weak neutral current interactions mediated by an uncharged boson, the so-called Z^0 boson. This prediction was later confirmed experimentally.

The theory has also been successful in predicting the existence of the gluon, the top-quark[2] and predicts the existence of a Higgs-boson. There is however some questions one may ask, which makes us think that the Standard Model can not be the final solution. The theory does not explain why the particles carry the masses which have been measured, and why the quarks and leptons exist in three generations. There is a large amount of parameters which are left undetermined and must be inserted by hand. If these parameters are truly determined by theory, one must find a still more fundamental theory which reduces to the Standard Model at presently explored energies and precisions. Some schemes predicts new physics

[1] A technique developed to deal with infinites in the theories.

[2] Fermilab's Tevatron measured the top-quark to have a mass 180 $\pm$ 12 GeV, spring 1995.

at the cutoff energy [2]

$$\Lambda \sim \frac{\sqrt{4\pi}M}{\sqrt{\alpha}}, \tag{1.2}$$

where M is the vector-boson mass. This cutoff is of order a few TeV, and represents the threshold energy for new physics. Future experiments such as the LHC (Large Hadron Collider), will cover this energy range and reveal the existence of new physics. However, particles that are too heavy to be openly produced at lower energies can affect the properties of the Z^0 boson through weak radiative corrections. The virtual presence of heavy physical states affect the theoretical predictions of the Standard Model in a calculable way. Thus, high precision measurements at presently available energies offer not only the opportunity to test the electroweak model, but also to look for departures due to new physics at energies beyond the range of what is available today.

When it comes to experimental precision tests of the electroweak model, e^+e^- annihilation processes at the energy of the Z^0 boson are ideal. Lots of physical observables sensitive to the electroweak couplings can be measured at very high accuracies from this process. An e^+e^- accelerator was therefore built at CERN during the 1980's, LEP. Four experiments have been operative in LEP since 1989. Tests are made by comparing cross-sections and asymmetries with the theoretical predictions for different centre-of-mass energies around the Z^0 resonance peak. Each successive year the precision of the Standard Model tests has improved thanks to the increase in the statistical and systematical precision of the measurements and also thanks to the improvements of the theoretical predictions [3]. A plot of the Z^0 mass and corresponding uncertainty as a function of time is shown in Figure 1.1.

The work of this thesis will cover some aspects of the luminosity measurement in the DELPHI experiment, mainly the weak contributions to the SAT visible Bhabha scattering cross section, which is described in Chapter 3. Experimental measurements of weak effects in low angle Bhabha scattering are performed. Effects on the Z^0 lineshape measurement due to the introduction of higher order weak contributions in the visible Bhabha cross section are examined. Results from both the experimental measurements and the effects on the Z^0 lineshape measurement are presented in Chapter 4. An introduction to the instruments used in the measurements is given in Chapter 2. But first, in the next section, an outline of the electroweak Standard Model is presented.

1.1 The Standard Model of electroweak interactions

One of the most profound insights in theoretical physics is that interactions are dictated by symmetry principles. The present belief is that all particle interactions

may be dictated by so-called local gauge symmetries.

The Standard Model of elecroweak interactions unifies electromagnetism and weak interactions. The gauge group of the theory is $SU(2)_T \times U(1)_Y$ which consists of the $SU(2)_T$ group of weak isospin, T, and the $U(1)_Y$ group of weak hypercharge, Y. Experiments show that only left-handed fermions are present in the charged weak currents. The left-handed component of the fermion fields of the i^{th} fermion family,

$$\psi_i = \begin{pmatrix} \nu_i \\ l_i^- \end{pmatrix} \quad \text{and} \quad \begin{pmatrix} u_i \\ d_i' \end{pmatrix}, \tag{1.3}$$

therefore transforms as $SU(2)_T$ doublets of weak isospin. $d_i' \equiv \sum_j V_{ij} d_j$ where V is the Cabibbo-Kobayashi-Maskawa mixing matrix. The right handed fields are $SU(2)_T$ singlets.

The $SU(2)_T$ structure of the weak currents leads to the an isospin triplet of weak currents

$$J_\mu^i = \bar{\psi}\gamma_\mu \frac{1}{2}\tau_i \psi, \quad \text{with} \quad i = 1, 2, 3, \tag{1.4}$$

where ψ denotes the isospin doublets in (1.3) and τ_i are the Pauli matrices. The $U(1)_Y$ gauge symmetry leads to the weak hypercharge current

$$j_\mu^Y = \bar{\psi}\gamma_\mu Y \psi, \tag{1.5}$$

where the weak hypercharge Y is defined by

$$Q = T^3 + \frac{Y}{2}, \tag{1.6}$$

where Q is the electromagnetic charge and T^3 is the third component of the weak isospin. That is,

$$j_\mu^{em} = J_\mu^3 + \frac{1}{2} j_\mu^Y. \tag{1.7}$$

The coupling of the weak isospin current to the weak isospin triplet W_μ^i, with $i = 1, 2, 3$ and coupling constant g, and the coupling of the weak hypercharge current to the singlet B_μ with coupling constant g', gives the interaction term in the Lagrangian this form [4]

$$\mathcal{L} = -ig(J^i)^\mu W_\mu^i - i\frac{g'}{2}(j^Y)^\mu B_\mu. \tag{1.8}$$

Since the presence of mass terms for gauge fields destroys the gauge invariance of the Lagrangian, the weak interactions, mediated by massive gauge bosons, raises a problem. The introduction of "spontaneous symmetry breaking" through the Higgs-mechanism, helps us, by making it possible to generate the mass of a particle without breaking the $SU(2)_T \times U(1)_Y$ gauge symmetry. The two fields

$$W_\mu^\pm = \sqrt{\frac{1}{2}}(W_\mu^1 \mp i W_\mu^2) \tag{1.9}$$

Boson	Mass (GeV)
γ	$< 3 \times 10^{-36}$
Z^0	91.187 ± 0.007
$W^{\pm}$	80.22 ± 0.26

Table 1.1: Gauge boson masses [5].

get massive by this spontaneous symmetry breaking and describe the two charged massive bosons $W^{\pm}$. The masses of these two bosons are

$$M_W = \frac{1}{2} v g, \tag{1.10}$$

where v is the vacuum expectation value of the Higgs field. The two neutral fields W^3_μ and B_μ mix in such way that the physical state

$$A_\mu = B_\mu cos\theta_W + W^3_\mu sin\theta_W, \tag{1.11}$$

is massless and the orthogonal state

$$Z_\mu = -B_\mu sin\theta_W + W^3_\mu cos\theta_W, \tag{1.12}$$

is massive. θ_W is called the Weinberg angle or weak mixing angle and is given by the ratio of the coupling constants of the two independent $SU(2)_T$ and $U(1)_Y$ groups

$$tan\theta_W = g'/g. \tag{1.13}$$

The mass of the Z^0 boson, which is represented by the Z_μ field, is given by

$$M_Z = \frac{1}{2} v \sqrt{g^2 + g'^2}. \tag{1.14}$$

The presently known boson masses can be seen in Table 1.1. By manipulating Eqn. 1.10, 1.13 and 1.14, it is easy to find the relation between the $W^{\pm}$ mass and the Z^0 mass to be

$$cos\theta_W = M_W/M_Z. \tag{1.15}$$

The inequality $M_Z \neq M_W$ is due to the mixing between W^3_μ and B_μ fields where it is required that the photon is massless. In the limit $\theta_W = 0$, we see that $M_Z = M_W$. The result (1.15) for M_W/M_Z is a prediction of the Standard Model with its choices in the Higgs sector. The parameter ρ, which specifies the relative strength between the neutral and charged current weak interactions, will due to Eqn. 1.15 be fixed to

$$\rho \equiv \frac{M^2_W}{M^2_Z cos^2\theta_W} = 1. \tag{1.16}$$

Fermion	Mass (MeV)
ν_e	$< 7.0 \times 10^{-6}$
e	0.511
u	2-8
d	5-15
ν_μ	< 0.27
μ	105.66
c	1000-1600
s	100-300
ν_τ	< 24
τ	1777.1 ± 0.5
t	$(180 \pm 12) \times 10^3$
b	4000-4500

Table 1.2: Fermion masses. All values is taken from [5], except the top mass value, which is an average of the CDF and DØ results [6], and the ν_τ limit [7].

An experimental measurement of the parameter ρ is therefore an interesting test of the electroweak theory.

A fermion mass term in the Lagrangian destroys, like a mass term in Eqn. 1.8, the gauge invariance of the Lagrangian. The same Higgs doublet which generates $W^\pm$ and Z^0 masses is however also sufficient to give masses to the leptons and quarks. The fermion masses are given by

$$m_f = \frac{G_f v}{\sqrt{2}}, \tag{1.17}$$

where G_f are the fermion coupling constants. These constants are unconstrained by theory and have to be determined through experimental measurements of the fermion masses. The presently known values of the fermion masses can be found in Table 1.2.

The weak neutral current J_μ^{NC} can be found from (1.8), (1.12) and by using the requirement (1.13):

$$J_\mu^{NC} \equiv J_\mu^3 - sin^2\theta_W j_\mu^{em}, \tag{1.18}$$

which relates the neutral current J^{NC} to the weak isospin current J. It is customary to express J_μ^{NC} in this form:

$$J_\mu^{NC} = \bar{\psi}\gamma^\mu \frac{1}{2}(c_v^f - c_a^f \gamma^5)\psi. \tag{1.19}$$

By comparing (1.18) and (1.19) one finds the vector and axial-vector couplings to be

$$c_v^f = T_f^3 - 2sin^2\theta_W Q_f, \tag{1.20}$$

$$c_a^f = T_f^3, \tag{1.21}$$

where T^3 and Q_f are the the third component of the weak isospin and the charge of fermion f, respectively.

The Standard Model has three free parameters which are not fixed by theory (neglecting the masses of the fermions and the Higgs-boson). In order to minimize the theoretical uncertainty on the predictions from the theory, it is clearly advantageous to choose physical inputs which are precisely measured. Two such precise inputs are the fine structure constant, α, determined from Thomson scattering [5],

$$\alpha = 1/137.0359895(61), \tag{1.22}$$

and the Fermi coupling constant, determined through measurement of the muon lifetime [5],

$$G_F = 1.16639(2) \times 10^{-5} GeV^{-2}. \tag{1.23}$$

For physics at the Z^0 resonance, the most natural choice of the third parameter is the Z^0 mass, where M_Z is obtained from a precise scan of the Z^0 resonance shape. With these parameters as inputs, predictions for other observables can be made and confronted with experiment.

Chapter 2

Instruments

The biggest research center in the world for nuclear and particle physics is CERN[1] near Geneva, Switzerland. The CERN organization was established in 1955 in an attempt to regain Europe's position in the forefront of scientific research which was lost during the Second World War. Today this European collaboration has 17 member states, among them Norway.

2.1 The LEP ring

The LEP[2] ring with colliding beams of electrons and positrons is the newest and most complex accelerator at CERN. It was built during the period 1983 to 1989 in a 27 km long circular tunnel and is the biggest colliding beam accelerator in the world. It was designed to accelerate electrons to an energy around 45.5 GeV and then to store the electron-bunches at this energy. This gives a centre-of-mass energy of 91 GeV which is ideal for Z^0 production. Of eight interaction points in the ring, four are strongly focused and equipped with detectors. These four detectors (experiments) have been operative since August 1989 and have detected over 4 millions Z^0 decays each produced by LEP.

The LEP ring is soon going to be upgraded to run at higher beam-energies of somewhere between 90-100 GeV[3]. LEP is then changing name to LEP2. One of the tasks for LEP2 is to produce particles which could reveal the existence of a Higgs-boson. A feature which is important to consider with LEP2 is the synchrotron energy loss. For a particle of charge e, velocity $v = \beta c$, and energy $E = \gamma mc^2$, traveling in a circular orbit of radius R, the energy loss per revolution δE is [5]

$$\delta E = \frac{4\pi}{3}\frac{e^2}{R}\beta^3\gamma^4. \tag{2.1}$$

[1]Conseil Europeen pour la Recherche Nucleaire. Today the official name is European Organization for Nuclear Research, but the old acronym is still used.

[2]Large Electron Positron collider.

[3]LEP raised its beam-energy to 65 GeV on October 30, 1995.

For high-energy electrons ($\beta = 1$), this becomes:

$$\delta E(GeV) = 88.5 \times 10^{-6}[E(GeV)]^4/R(m). \tag{2.2}$$

If we use these formulae for the LEP and LEP2 beam-energies, we see that the LEP2 energy loss will be about 20 times the LEP energy loss. In LEP2 this electron loss must therefore be compensated by installation of super-conducting RF-cavities for acceleration and installation of an improved cooling system.

2.2 DELPHI

DELPHI[4] is one of the four experiments in the LEP ring. The other three are ALEPH, L3 and OPAL. The DELPHI detector [8] consists of many sub-detectors with various tasks. LEP produces a great variety of particles in the collisions and different particles usually require different detectors to be seen. All the different sub-detectors are therefore needed to detect these different particles. A short description of some of the most important sub-detectors follows (the luminosity monitors are described in some greater detail in the next sections).

Hadron calorimeter Used for measuring the energies of hadrons. A hadron calorimeter is necessary for the detection of neutral hadronic particles. The detector consists of a barrel and a end-cap section.

High density projection chamber (HPC) A barrel electro-magnetic calorimeter used for determining electron and photon energies. When a shower develops inside a module, it ionizes the gas. The freed electrons drift towards the end of each gap, where they are detected by a proportional chamber.

Time projection chamber (TPC) Used for finding particle momenta and charge. A charged particle crossing the gas volume creates an ionization path along its track. The ionization path drifts towards a multi-wire proportional chamber due to the longitudinal electric field. The magnetic fields bends the trajectories for momentum determination.

Barrel RICH The Ring Imaging Cherenkov counter is used to identify hadrons. Whenever the velocity of a charged particle exceeds c/n (n is the refractive index of the medium), Cherenkov light is produced. It can be shown that the light will travel relative to the particle-axis at an angle θ given by

$$cos\theta = \frac{1}{\beta n}. \tag{2.3}$$

By measuring θ, β can be found, and with the use of TPC the momentum is found and since $\beta = p/E$, the particle mass can be determined.

[4] DEtector for Lepton, Photon and Hadron Identification.

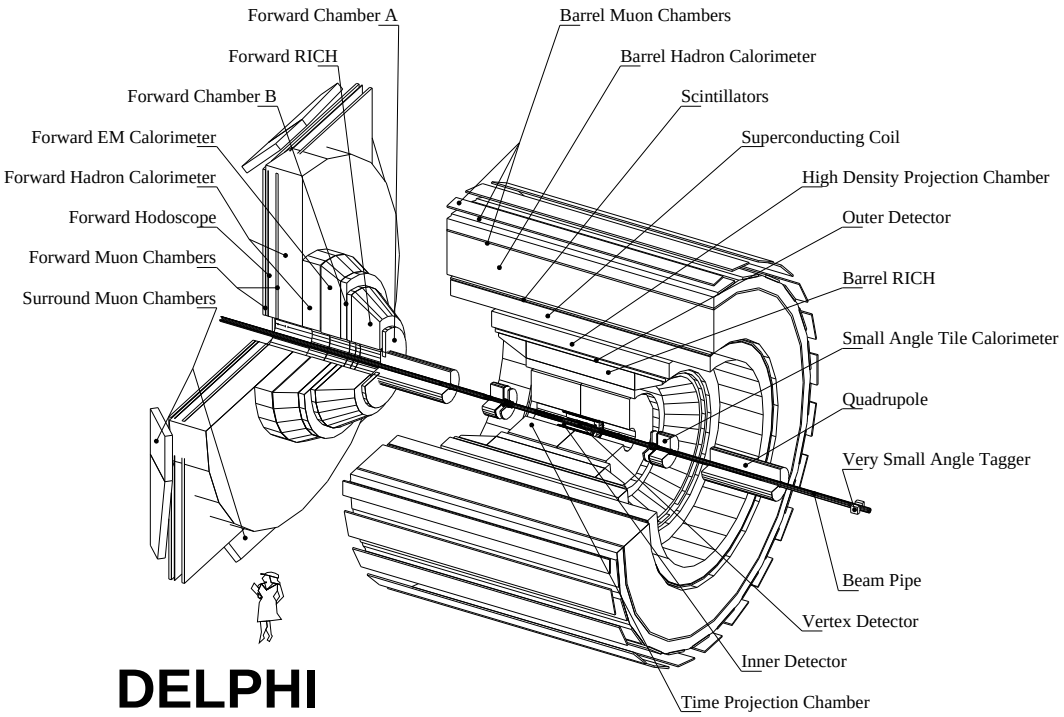

Figure 2.1: The DELPHI detector.

Micro-vertex detector Placed very close to the interaction point. Gives high precision measurements of charged tracks close to the beam pipe.

2.3 The DELPHI Coordinate System

In this thesis the following definition of the DELPHI coordinate system is used:

x: Horizontal, pointing towards the LEP centre.

y: Up.

z: Along beam, anticlockwise (as viewed from above), that is, parallel to the electron beam.

The corresponding spherical coordinates are defined by

$$\begin{aligned} x &= r sin\theta cos\phi, & 0 \leq \phi \leq 2\pi \\ y &= r sin\theta sin\phi, & 0 \leq \phi \leq \pi \\ z &= r cos\theta, \end{aligned}$$

where r is the distance from the origin.

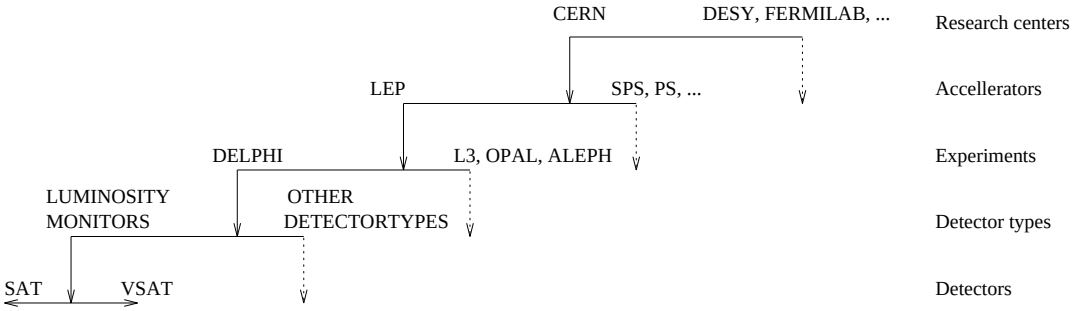

Figure 2.2: The SAT detector's place in the hierarchy of experimental particle physics.

2.4 SAT

The SAT[5] detector consists of electro-magnetic calorimeters installed on both sides of the interaction point and a tracker unit of 2 planes in front of one of the calorimeters. It is made for luminosity monitoring through the detection of Bhabha-scattering. The calorimeters covers scattering angles between approximately 43 and 135 mrad corresponding to a visible cross section of about 27 nb after selection cuts. The importance of the forward region for luminosity monitoring is discussed in the next chapter. The detector is also used for identification of reactions which are backgrounds for interesting processes. Such a background process can be radiative Bhabha scattering, where the final-state electrons remain near to the beam pipe and is a background to neutrino counting through the process $e^+e^- \rightarrow Z^0\gamma \rightarrow \nu\bar{\nu}\gamma$.

Figure 2.1 shows where SAT was placed in the DELPHI experiment, it was situated approximately where STIC can be seen in the figure. Figure 2.2 shows the SAT detector's place in the hierarchy of experimental particle physics.

The segmentation of one half barrel is shown in Figure 2.3. From the figure we can see that the calorimeter consists of eight rings where the inner six have radial extensions of 3.00 cm and the two outermost 3.25 cm. The inner ring starts at a radius of 10 cm and the outer ends at 34.5 cm. The Φ segmentation is 15.0 degrees in the inner four rings and 7.5 degrees in the outer four. The active part of the calorimeter modules are located at z-position between 232 cm and 272 cm. A set of lead masks were installed in front of one of the calorimeters to define a precise acceptance region. A second mask, the ϕ mask, covers the junction in the vertical plane of the two halves of the masked calorimeter. More information of the calorimeter can be found in references [8, 9].

The tracker unit of 2 planes was installed in front of the SAT calorimeter on

[5]Small Angle Tagger

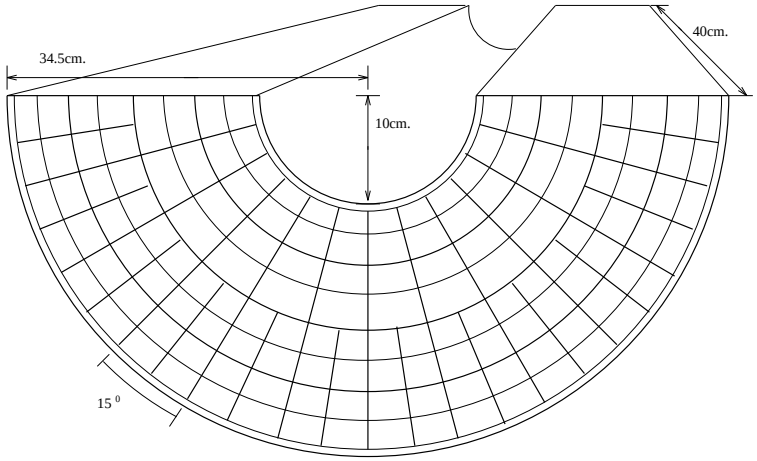

Figure 2.3: The SAT calorimeter.

side A, opposite the masked calorimeter in arm C. The two planes are located at z = -230.0 and -202.7 cm. The sensitive region extends from 43.3 to 120.3 mrad, and the inner radii of both planes are 9.95 cm. For the 1993 running the use of the tracker data allowed a considerable reduction in the systematic error due to the definition of the fiducial region in the unmasked calorimeter. More information about the SAT tracker can be found in [10].

When space around the SAT was freed up due to the installation of a beam-pipe with a smaller radius, the decision was made to replace SAT with a new luminosity monitor. The replacement took place during the spring in 1994 and the new detector is described in the following section.

2.5 STIC

The STIC (Small angle TIle Calorimeter) detector was installed before the 1994 LEP run. It consist of two lead scintillator sampling calorimeters, each divided into two halves for a total of four modules. It is located in DELPHI at 2200 mm from the interaction point, covering an angular region from 29 to 188 mrad, with a front radius between 65 and 417.5 mm [11] corresponding to a visible cross section of about 60 nb after selection cuts. The calorimeters consist of 47 lead/scintillator layers and two planes of Si detectors. The two planes of Si strip detectors are installed because the detector should be able to measure the direction of a shower with a $\sim$10 mrad accuracy to improve the rejection of off momentum electrons. A tungsten ring (for the same purpose as the lead mask with SAT) is also used with STIC but in addition radial position measurements with this new detector makes it possible to define other smaller acceptance regions

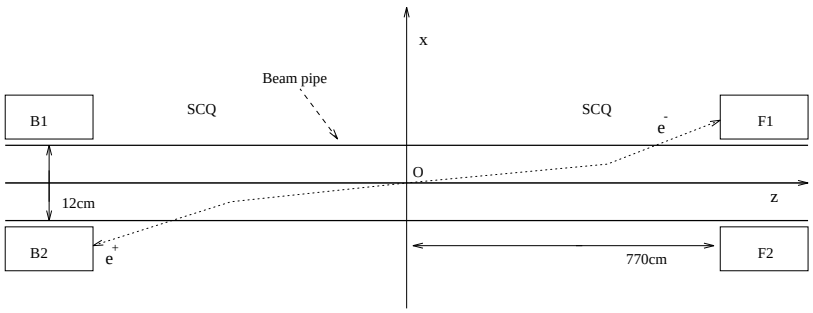

Figure 2.4: Layout of the position of the VSAT modules with respect to the DELPHI origin.

and determine the luminosity without using the tungsten ring, thus providing an (almost) independent luminosity measurement. The major improvements with respect to the SAT luminometer can be summarized as follows:

1. A very good energy resolution allows for an easy separation of Bhabha scattering events from the background due to off momentum particles from beam-gas interactions.

2. The accuracy in the definition of the internal geometry of the detector, the absence of discontinuities and the good spatial resolution allow for a very precise definition of the geometrical acceptance.

2.6 VSAT

The VSAT (Very Small Angle Tagger) is also an electro-magnetic calorimeter for the luminosity measurement in DELPHI. It is composed of four modules adjacent to the beam pipe, in the elliptical section located at 7.7 m from the interaction point (further away from the IP than the super-conducting quadropoles (SCQ)), two in the forward region and two in the backward region (Figure 2.4). The distance between two neighboring modules is about 12 cm. The dimensions of the four calorimeters, composed of planes of detectors and tungsten blocks, are 3 cm in the transverse horizontal direction (x), 5 cm in the vertical direction (y) and about 10 cm along the beam direction (z). Due to the very small emission angle of the Bhabha events accepted in the VSAT, in spite of the restricted angular acceptance of the detector which is between 5 and 7 mrad in polar angle and 180 degrees in azimuth, the accepted Bhabha cross section is very large, about 500 nb. Due to the defocusing effect of the SCQ magnets, the visible cross section will be larger than the visible cross section in the angular acceptance between 5 and 7 mrad, Bhabhas with somewhat smaller angles (before they reach the

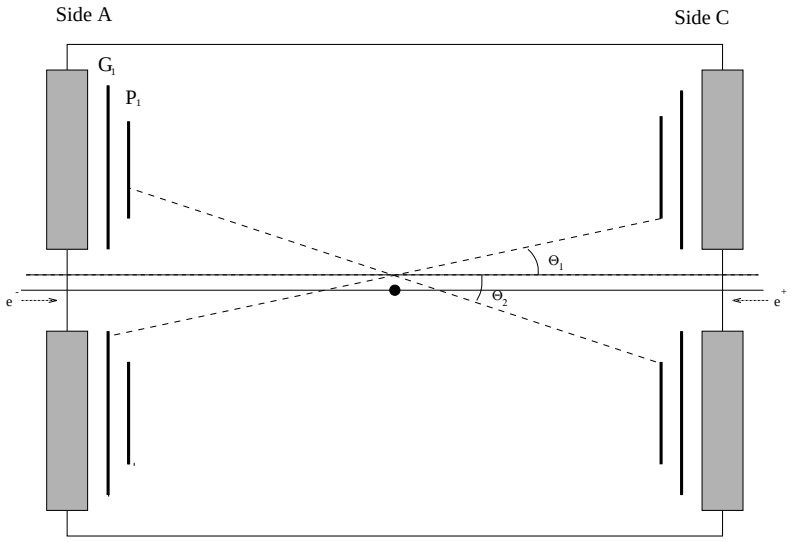

Figure 2.5: Diagram illustrating the principle of asymmetric acceptances. The solid horizontal line shows the nominal beam axis and the dashed line parallel to this axis is an arbitrary radially displaced beam axis. The dashed lines not parallel to the beam axis, show the projection of the inner radius of the "inner" acceptance region in arm C through a vertically displaced IP to arm A.

SCQ) will also be monitored. That is, the effective distance from the center of DELPHI to the VSAT modules will increase [13]. The large cross section allows the luminosity to be monitored with high statistics. The energy measurement of the shower produced inside the modules is made using the signals of 11 silicon Full Area Detectors (FAD), whereas the shower position is measured using 3 silicon strip planes, with a pitch of 1 mm, placed at 5, 7 and 9 radiation lengths. More details are given in references [14, 15].

2.7 Beam displacements

The center of the DELPHI detector is defined as the center of the TPC. Several detectors (Micro-vertex detector, VSAT) measure the beam interaction point (IP) relative to this centre. The IP position varies with time and it is necessary to study how the detector acceptances are affected by this and find methods to reduce the effects on the visible cross section caused by these IP-displacements. A well-established method of defining an asymmetric geometric acceptance in a pair of identical detectors placed symmetrically about the IP can be used to minimize the sensitivity of the acceptance to the properties of the IP [16]. Figure 2.5 illustrates the principle of this method.

From this figure we see that a vertical displacement of the IP from its nominal position (the center of DELPHI), the minimum scattering angle in the top, right "inner" counter, θ_1, is reduced while the minimum scattering angle into the bottom, right "inner" counter, θ_2, is increased. The net effect is a lowest order cancelation in the sum of the changes to the visible cross-section. For longitudinal displacements of the IP the use of the acceptance mask technique in SAT prevents the longitudinal symmetrization of the acceptance. This results in an uncompensated first order dependence of the acceptance to the z-position of the IP [17]:

$$\frac{1}{\sigma_0}\frac{\Delta\sigma}{\Delta z} = (-0.754 + -0.002)\%/cm, \tag{2.4}$$

where σ is the measured cross section, Δz the longitudinal displacement, σ_0 is the cross section at $\Delta z = 0$ and $\Delta\sigma$ the correction on the cross section due to the longitudinal displacement. Figure 2.6 shows how the SAT detector acceptance depend on various beam parameters [17].

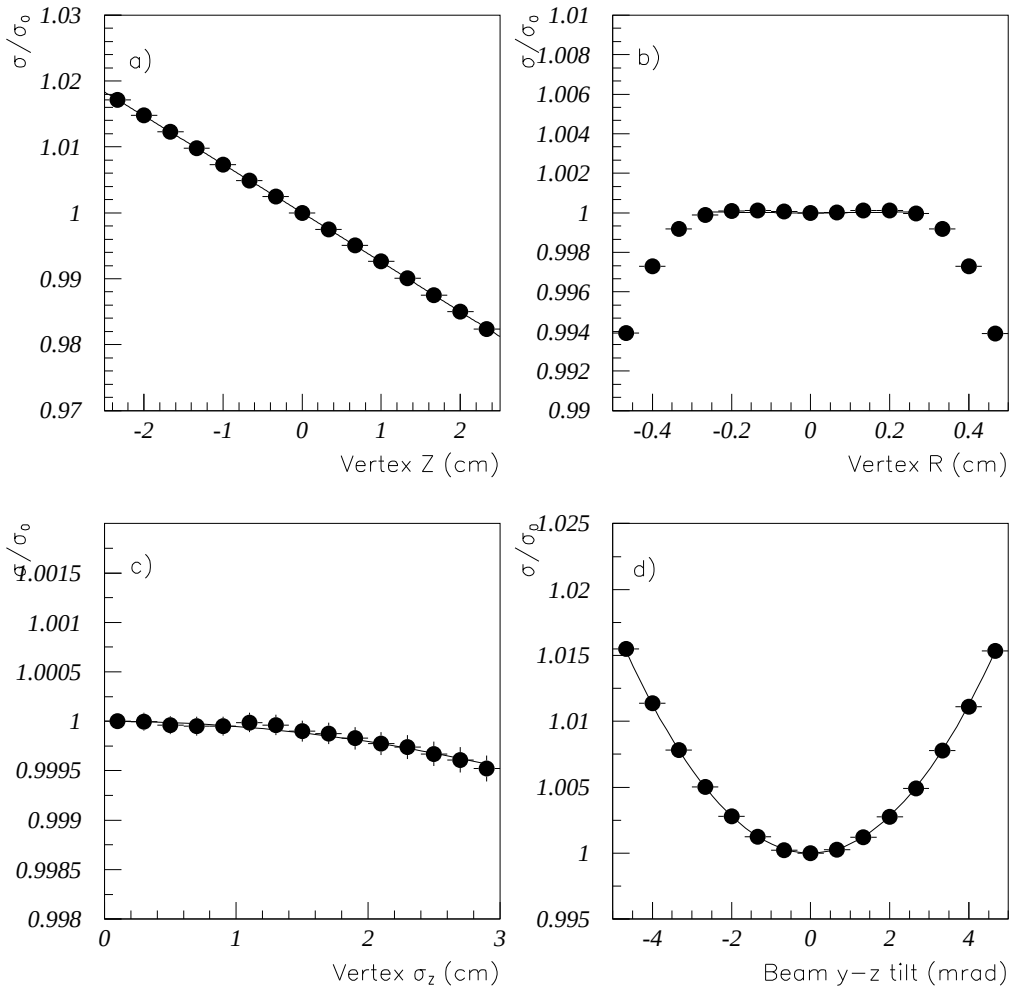

Figure 2.6: Dependence of the SAT detector acceptance, σ/σ_0, on the longitudinal (a) and radial (b) displacements of the IP, and on the longitudinal spread of the IP (c), and on the beam x-y tilt (d).

Chapter 3

Luminosity

A cross section is measured by using the formula

$$\sigma_x = \frac{N_x}{L}, \tag{3.1}$$

where N_x is the number of events produced in any reaction x, and σ_x is the cross section for that process. The integrated luminosity, L, is defined as

$$L = \int \mathcal{L}\mathrm{dt} = \frac{\mathrm{N_x}}{\sigma_\mathrm{x}}. \tag{3.2}$$

It is important to know the beam-luminosity in an experiment at a high level of accuracy if one is going to measure any cross-section precisely. The luminosity measurement at LEP consists of counting the number of events produced by Bhabha scattering detected within a certain acceptance and dividing by the theoretical cross section into that acceptance. An accurate determination of absolute cross sections for other processes can therefore be achieved with a high precision measurement of the luminosity. Bhabha scattering is a process one has found suitable for the determination of the luminosity due to its high cross section at low angles and its well known theory. The theory is however not trivial because the present LEP luminometer precisions is very high and contributions to the cross section from weak and higher order effects are therefore non-negligible. Lowest order QED calculations do thus not suffice.

3.1 Present experimental errors on the luminosity measurement at LEP

Recently the LEP Collaborations have all made significant progress in reducing the pure experimental error in their luminosity measurements. Some of them have reached a precision better than 0.1 % in this error. By the replacement of SAT by STIC, the experimental error in the DELPHI luminosity measurement

was reduced from 0.24 % to 0.09 % [18]. The theoretical predictions of these measurements must therefore be improved to the same below 0.1 % regime in order to avoid letting the theoretical errors unnecessarily impede the high precision tests of the Standard Model.

In the rest of this chapter I will present a formulae for calculation of the lowest order QED and EW Bhabha cross section and show plots of these and of some $O(\alpha)$ and higher-order contributions to the weak cross section.

3.2 Bhabha Scattering

By elastic Bhabha Scattering one means the process

$$e^+e^- \rightarrow e^+e^- \tag{3.3}$$

where only an e^+e^- pair is detected in the final state. This process never occurs, as the process is always accompanied by the emission of electro-magnetic radiation. This is called Radiative Bhabha Scattering

$$e^+e^- \rightarrow e^+e^-\gamma \tag{3.4}$$

where an additional photon is also produced. A Bhabha event in the forward direction can be seen in Figure 3.1.

3.2.1 The QED Cross Section

The Feynman diagrams in Figure 3.2 visualize lowest order QED Bhabha scattering. The electron and positron interact by exchanging either a space-like or a time-like photon-propagator. At LEP energies, where the electron mass can be neglected, the centre-of-mass differential cross section is found to be [19]

$$\frac{d\sigma_0^{QED}}{d\Omega} = \frac{\alpha^2}{4s}\left((1+c^2) + 2\frac{(1+c)^2+4}{(1-c)^2} - 2\frac{(1+c)^2}{1-c}\right), \tag{3.5}$$

where $c = cos\theta$, s is the centre-of mass energy squared and $d\Omega$ is the solid angle element $dcos\theta d\phi$. The angles θ and ϕ are defined as the polar and azimuthal scattering angles of the positron. The three terms in the formula correspond to the annihilation diagram, the exchange diagram and the interference term, respectively. This formula can be reduced to a simpler form:

$$\frac{d\sigma_0^{QED}}{d\Omega} = \frac{\alpha^2}{4s}\left(\frac{3+c^2}{1-c}\right)^2. \tag{3.6}$$

Figure 3.3 shows how the differential cross section varies as a function of θ and the centre-of-mass energy. When the polar angle is small, $\theta \ll 1$, we can write

$$\frac{d\sigma_0^{QED}}{d\Omega} \simeq \frac{16\alpha^2}{s}\frac{1}{\theta^4}. \tag{3.7}$$

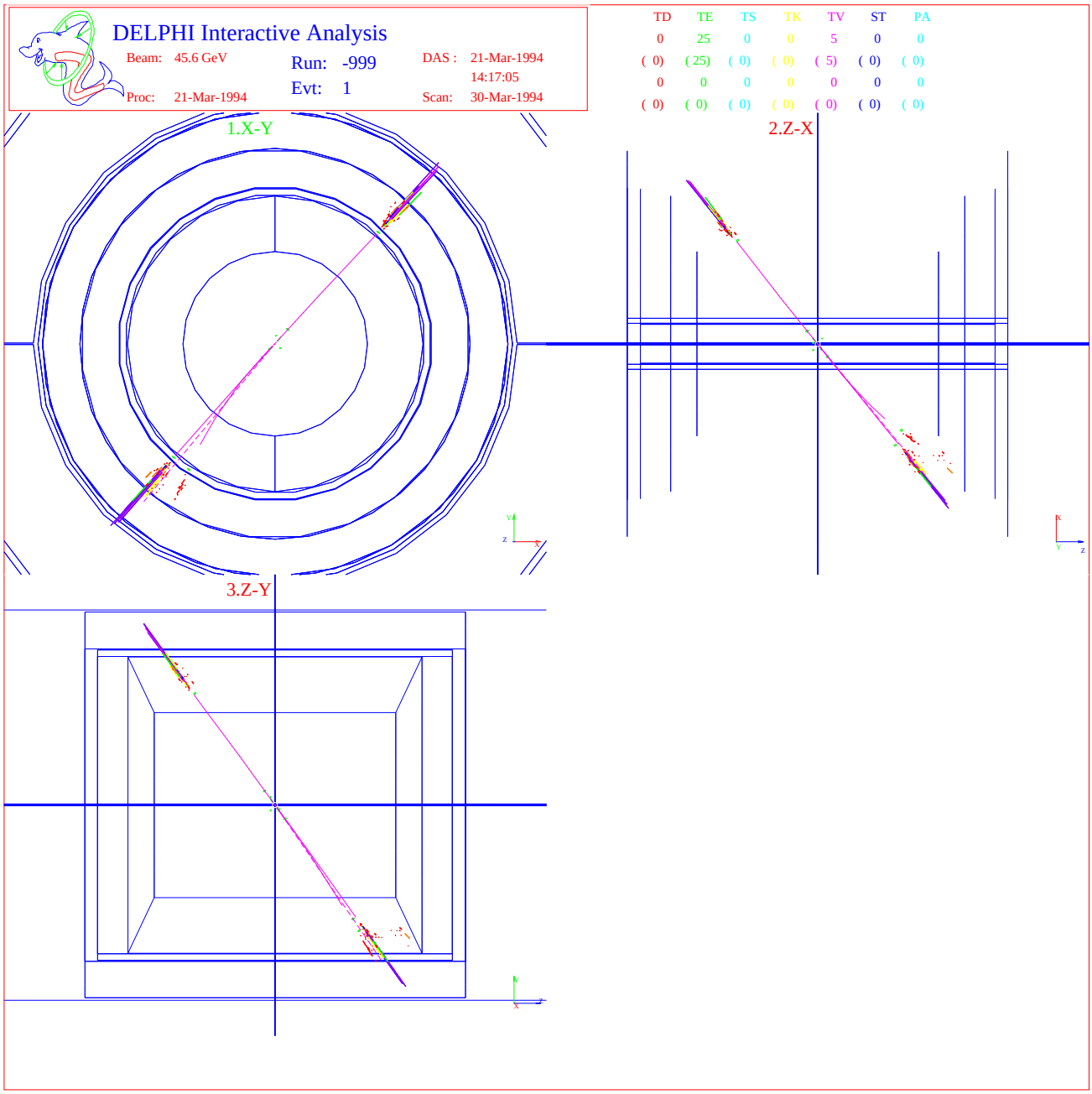

Figure 3.1: A Bhabha event in the forward directions seen in the X-Y, Z-X and Z-Y plane.

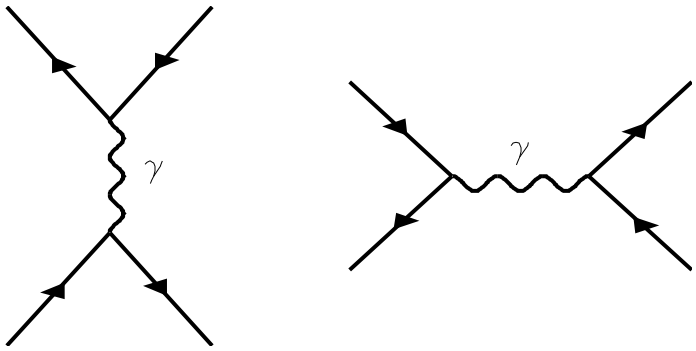

Figure 3.2: Feynman diagrams for the lowest order QED Bhabha scattering.

This formula clearly shows how strongly the cross section depends on the scattering angle, θ. To find a integrated cross section, we can write the lowest order differential cross section as

$$\frac{d\sigma_0^{QED}}{d\theta} = \frac{32\pi\alpha^2}{s}\frac{1}{\theta^3}, \tag{3.8}$$

resulting in an integrated cross section of

$$\sigma_0^{QED} = \frac{16\pi\alpha^2}{s}\left[\frac{1}{\theta_{min}^2} - \frac{1}{\theta_{max}^2}\right], \tag{3.9}$$

where θ_{min} and θ_{max} define the outer limits of the acceptance. An uncertainty on the inner radius, R_{min}, of the acceptance, thus, induces an error on the estimated cross section, of

$$\frac{\Delta\sigma_0^{QED}}{\sigma_{QED}} \simeq 2 \times \frac{\Delta\theta_{min}}{\theta_{min}} \simeq 2 \times \frac{\Delta R_{min}}{R_{min}}. \tag{3.10}$$

The uncertainty of the SAT calorimeter geometry is 2-3 mm and this is why one has found it necessary to install a lead-mask in front of one of the calorimeters.

3.2.2 The Electro-weak Cross Section

As mentioned earlier, the contribution from the weak diagrams, shown in Figure 3.4 cannot be neglected in the luminosity measurement. The electro-weak differential cross section is found to be [19]:

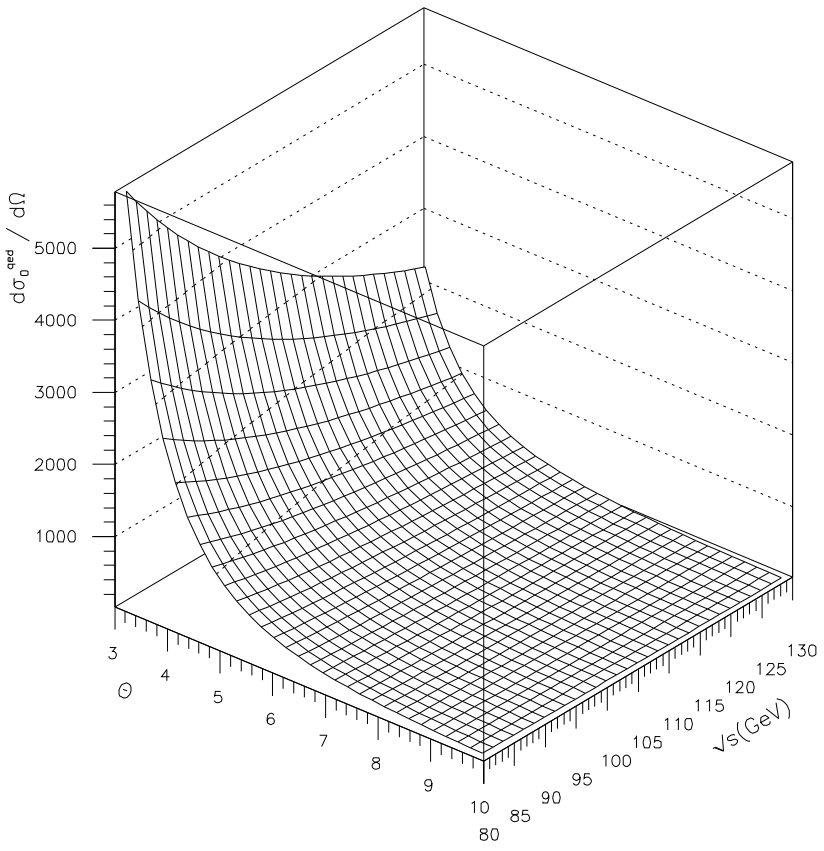

Figure 3.3: The differential lowest order QED cross section as a function of the polar scattering angle, θ, and the centre-of-mass energy.

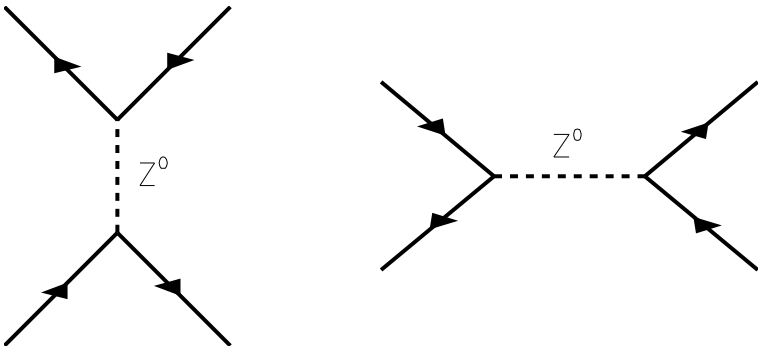

Figure 3.4: Feynman diagrams for the lowest order weak Bhabha scattering.

$$\frac{d\sigma_0^{EW}}{d\Omega} = \frac{\alpha^2}{4S}\Big(S^{\gamma\gamma}(s,s) + 2ReS^{\gamma\gamma}(s,t) + S^{\gamma\gamma}(t,t) + 2ReS^{\gamma Z}(s,s) + 2ReS^{\gamma Z}(s,t) + 2ReS^{\gamma Z}(t,s) + 2ReS^{\gamma Z}(t,t) + S^{ZZ}(s,s) + 2ReS^{ZZ}(s,t) + S^{ZZ}(t,t)\Big) \tag{3.11}$$

where the S^{ij} are defined by

$$S^{ij}(s,s) = \Big[F^{ij}(1+c^2) + G^{ij}(2c)\Big]\chi_i^*(s)\chi_j(s) \tag{3.12}$$

$$S^{ij}(s,t) = -\Big[F^{ij} + G^{ij}\Big]\left[\frac{(1+c)^2}{1-c}\right]\chi_i^*(s)\chi_j(t) = S^{ij}(t,s) \tag{3.13}$$

$$S^{ij}(t,t) = 2\Big[F^{ij}\Big[(1+c)^2+4\Big] + G^{ij}\Big[(1+c)^2-4\Big]\Big]\frac{\chi_i^*(t)\chi_j(t)}{(1-c)^2} \tag{3.14}$$

and

$$F^{ij} = (v^i v^j + a^i a^j)^2, \qquad G^{ij} = (v^i a^j + a^i v^j)^2 \tag{3.15}$$

where $a^\gamma = 0$, $v^\gamma = 1$, $a^z = \frac{-1}{4s_w c_w}$, $v^z = (1-4s_w^2)a^z$, $c = cos\theta$ and $t = -s/2(1-c)$.

$$\chi_z(s) = \frac{s}{(s-M_z^2) + iM_z\Gamma_z}, \qquad \chi_\gamma(s) = 1. \tag{3.16}$$

To see how the weak terms contribute to the cross section, we can write 3.11 as

$$\frac{d\sigma_0^{EW}}{d\Omega} = \frac{d\sigma_0^{QED}}{d\Omega}(1+\delta_w) \tag{3.17}$$

and δ_w will contain the weak effect. Figure 3.5 shows δ_w as a function of centre-of-mass energy and scattering angle. We see that the weak effect has a peak at

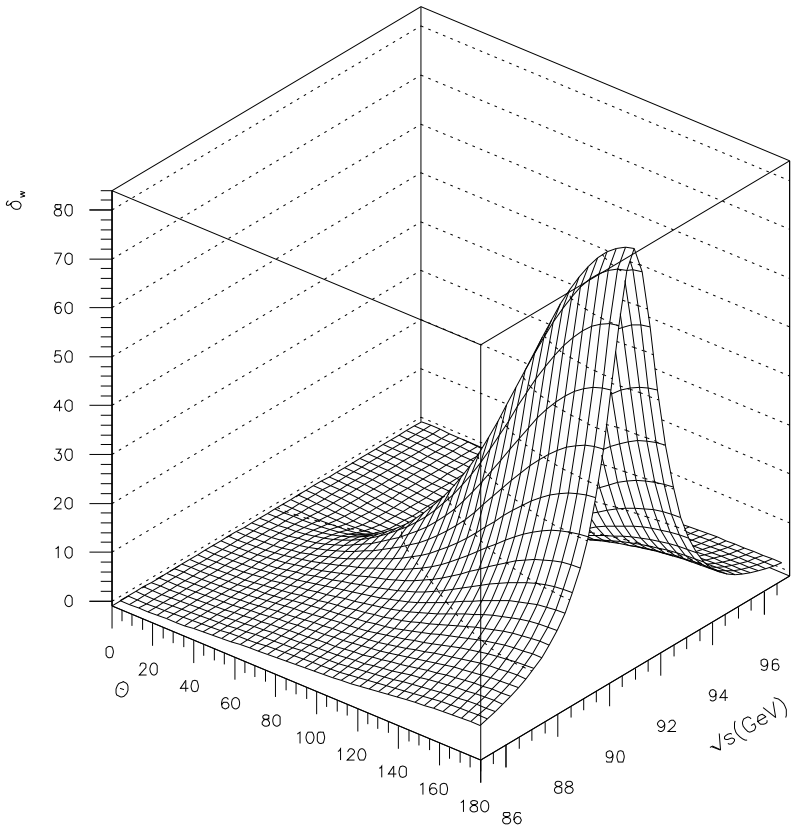

Figure 3.5: The weak correction to the Bhabha cross section as a function of center-of-mass energy and scattering angle, θ.

the Z^0 resonance and that it grows fast with the scattering angle. The weak effect originates mainly from the Z^0 annihilation channel and the interference between this and the photon channels. Figure 3.6 shows the same cross section as Figure 3.5, but now in greater detail at low scattering angles, which is the interesting area for luminosity-monitoring. At these low angles, the photon exchange channel contribution is huge, and the weak contribution is therefore rather small compared with larger angles. We see that the weak terms have a positive contribution below the Z^0 resonance and a negative contribution above and form a typical pattern around the Z^0 resonance. This pattern mainly originates from the interference between the γ_t and Z_s terms. On top of the Z^0 resonance however, the weak effect is barely seen at these angles. This can be explained from Eqn. 3.13, where it can be seen that the interference terms are imaginary at the top of the Z^0 resonance.

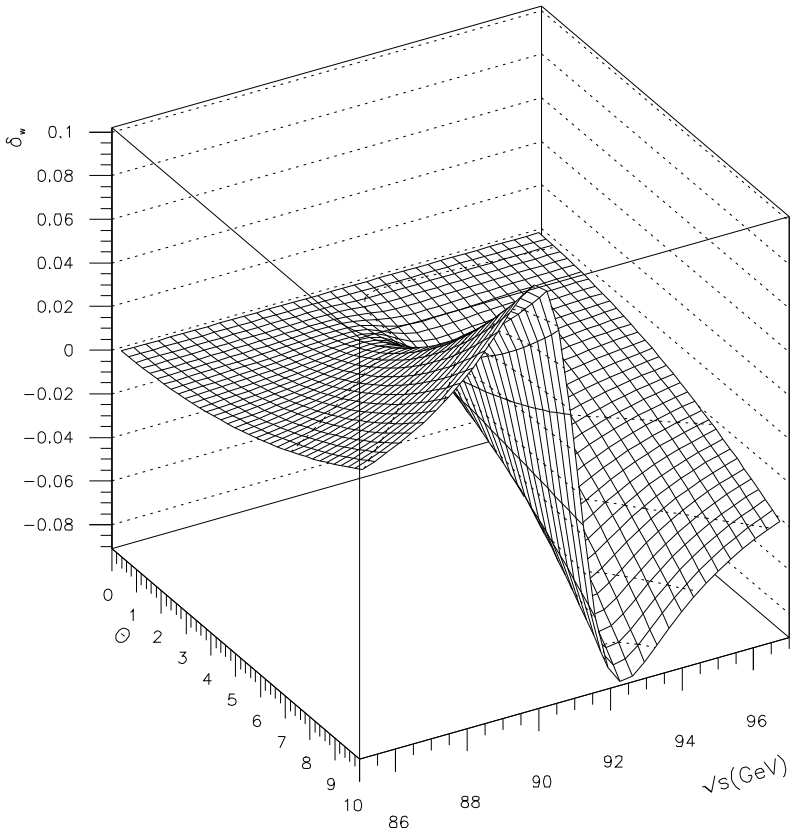

Figure 3.6: The weak correction to the Bhabha cross section as a function of center-of-mass energy and scattering angle, θ, at small scattering angles.

3.2.3 QED corrections to the lowest order Bhabha cross section

As shown earlier in this chapter, the lowest order QED expression for the Bhabha scattering cross section is very simple (3.6). The higher order cross section is however more complicated and depends on the interplay between final states with one or more additional photons and the experimental cuts. The method used to find an estimated cross section is therefore based on Monte Carlo simulation techniques, where events are produced by an event generator and passed through a detailed detector simulation program. After analyzing these events the same way as real data, the number of events remaining inside the detector acceptance then gives the theoretical cross section. The cross section precision will therefore depend on the number of simulated events. The events, used to find the SAT theoretical cross section, were produced at a fixed centre-of-mass energy of $\sqrt{s} = M_Z$, where M_Z was fixed to 91.1 GeV. The weak effects was taken care of by the BABAMC event generator [20] which is a full $O(\alpha)$ Bhabha scattering MC program containing Z^0-exchange terms. Today the Monte Carlo event generator BHLUMI V4.02 [22, 23], which contains weak $O(\alpha)$ and Leading Log (LL) higher order corrections, is used to find the SAT visible cross section.

The total QED contribution (without any weak effects) to the Bhabha cross section varies like $\sim 1/s$, similar to the lowest order QED contribution (3.9). Energy-dependent contributions on the lowest order QED cross section will therefore come from weak effects and can be extracted from relative Bhabha cross sections at different energies without knowing any details of the QED contributions other than the lowest order dependence. QED corrections to the lowest order QED cross section are therefore not treated here. Information on these corrections can be found in references [20, 21, 22].

3.2.4 O(α) corrections to the terms containing Z-boson exchange

The limiting factor in the luminosity precision has until 1992-93 been the luminometers and a very detailed calculation of the theoretical cross section has therefore not been necessary. But recently the luminometers have become more precise (SAT replaced by STIC spring '94) and an improved theoretical calculation was needed. To understand this we have to remember that the precision of LEP luminometers was originally planned around 1%. With this precision, the lowest order weak contributions to the cross section would suffice in the theoretical calculation. But with the present luminometer-precision of less than 0.1%, weak $O(\alpha)$ corrections has to be included in the calculations together with leading higher-order corrections. A great effort in achieving this has been done and work is still in progress [23].

To get a clearer picture and to see the importance of the $O(\alpha)$ corrections,

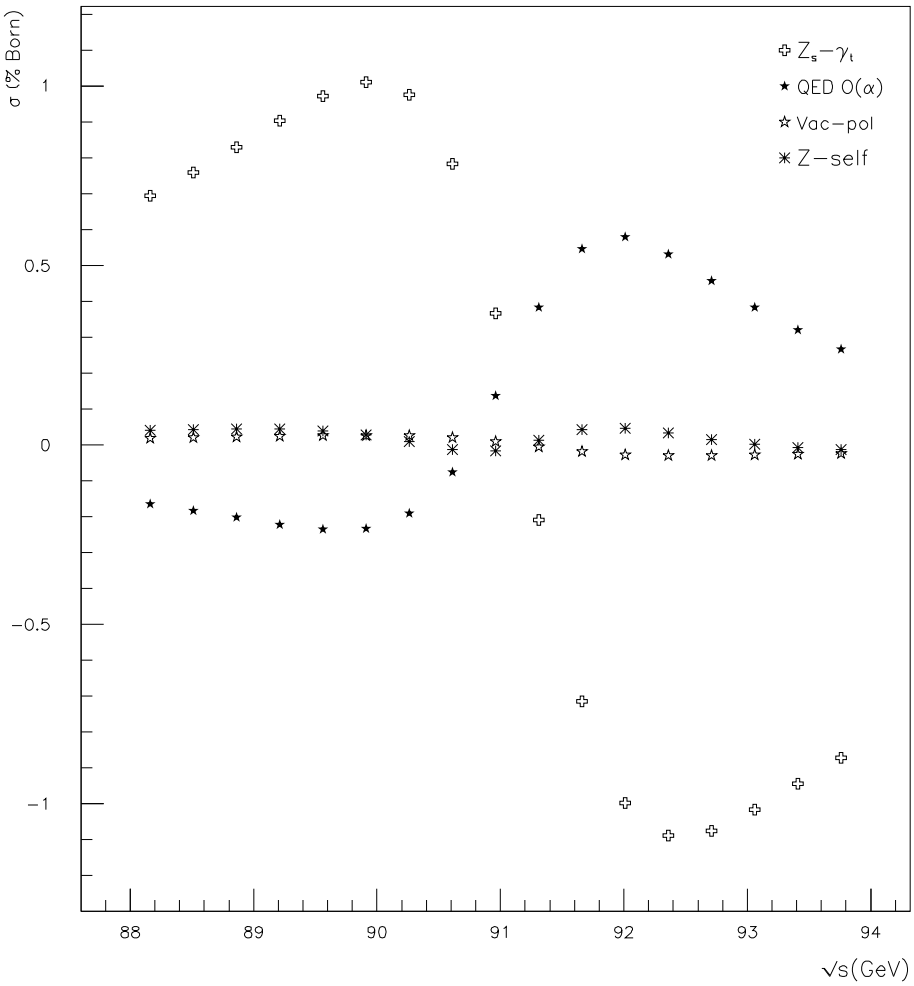

Figure 3.7: Z-boson exchange contributions calculated from the formulae in [24] and presented as fraction (%) of the Born cross section in the symmetric angular region between 3.2^o and 7.3^o. The corresponding numerical values are presented in Table 3.1.

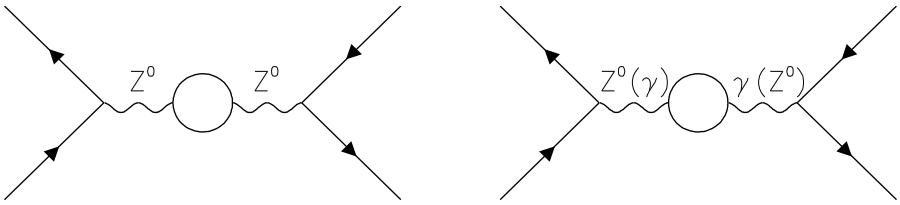

Figure 3.8: Z^0 self energy Feynman diagrams contributing to the weak corrections to Bhabha scattering.

Figure 3.7 shows the most important contributions, together with the lowest order weak contribution, in percent of the Born cross section, in the symmetric angular region between 3.2 degrees and 7.3 degrees, which approximates the SAT acceptance. All the contributions in Figure 3.7 together represent the entire Z contribution as calculated in $O(\alpha)$. This can be split into the lowest order "Z-born" (Z_s-γ_t-interference) and the "$O(\alpha)$ correction" which is the rest of the graphs. The "QED $O(\alpha)$" represents the pure bremsstrahlung (photonic) part of the "$O(\alpha)$ correction" and the remaining graphs denotes the rest of the "$O(\alpha)$ correction", that is, all kinds of vacuum polarizations and self-energies. Figure 3.9 shows some Feynman diagrams of the "QED $O(\alpha)$" contributions and Figure 3.8 shows the Z^0 self energy Feynman diagrams. An approximate formulae is used to calculate these contributions [24] and describes the results of the Monte Carlo program BABAMC and the semi-analytical program ALIBABA[1] [25] (without the leading higher-order corrections)[2] with a precision of 0.07 % of the full Born cross-section.

As can be seen from Figure 3.7, the QED $O(\alpha)$ corrections to the Z-boson exchange contributions above the Z^0 resonance, can reach 50 % of the peak value at lowest order, whereas the remaining $O(\alpha)$ corrections are rather small (below 0.05% of the Born cross section).

3.2.5 Leading higher-order contributions to the terms containing Z-boson exchange

The same formulae [24] are also used to calculate the leading higher-order terms and describe the results of ALIBABA[3] with a precision of 0.06 %. Figure 3.10

[1] ALIBABA: A semi-analytical program, containing Z-exchange contributions, that calculates full $O(\alpha)$ corrections and in addition re-summation effects and higher-order multi-photon QED corrections in the leading-log approximation.

[2] Leading higher-order corrections are originally present in ALIBABA.

[3] Now with leading higher-order contributions.

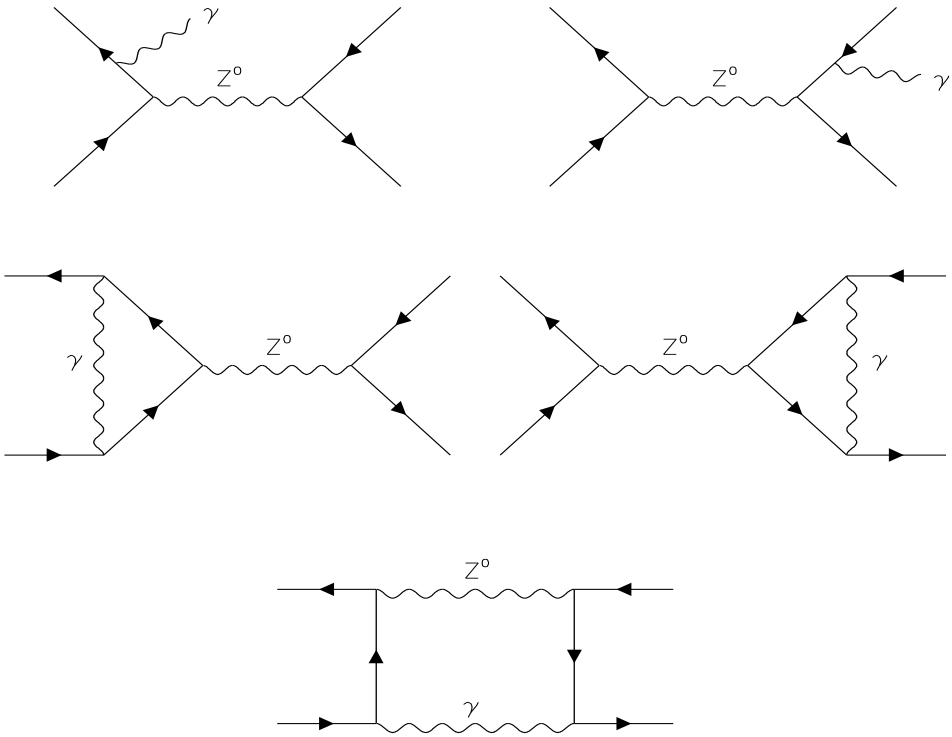

Figure 3.9: Feynman diagrams with Z^0 boson exchange which contribute to the photonic corrections to Bhabha scattering.

Energy (GeV)	Z-born	QED O(α)	Vacuum Pol.	Z self-energy	Higher-order
89.661	+0.991	-0.237	+0.027	+0.037	+0.861
90.036	+1.010	-0.221	+0.027	+0.021	+0.891
90.411	+0.905	-0.144	+0.024	-0.002	+0.837
90.786	+0.572	+0.036	+0.015	-0.018	+0.622
91.161	+0.000	+0.300	+0.000	+0.000	+0.229
91.536	-0.591	+0.514	-0.016	+0.037	-0.201
91.911	-0.956	+0.582	-0.026	+0.048	-0.504
92.286	-1.085	+0.542	-0.029	+0.035	-0.653
92.661	-1.077	+0.463	-0.029	+0.017	-0.702

Table 3.1: Some numerical values of the plots in Figure 3.7. Each column represent different contributions in % of the Born cross section. The last column represent the total weak contribution including higher order corrections to the Born cross section.

shows the contribution from these terms that is added to the $O(\alpha)$ calculation in BABAMC, and the full weak corrections including higher-order contributions can be seen in the last column of Table 3.1.

From Figure 3.10 we see that the higher order terms contribute with an $\sim$0.1% effect at the Z-peak. BABAMC calculates the weak corrections only to $O(\alpha)$. The current SAT QED uncertainty is 0.16% and the weak higher order contributions is therefore nedded in the calculation of the SAT visible cross section to minimize the total error.

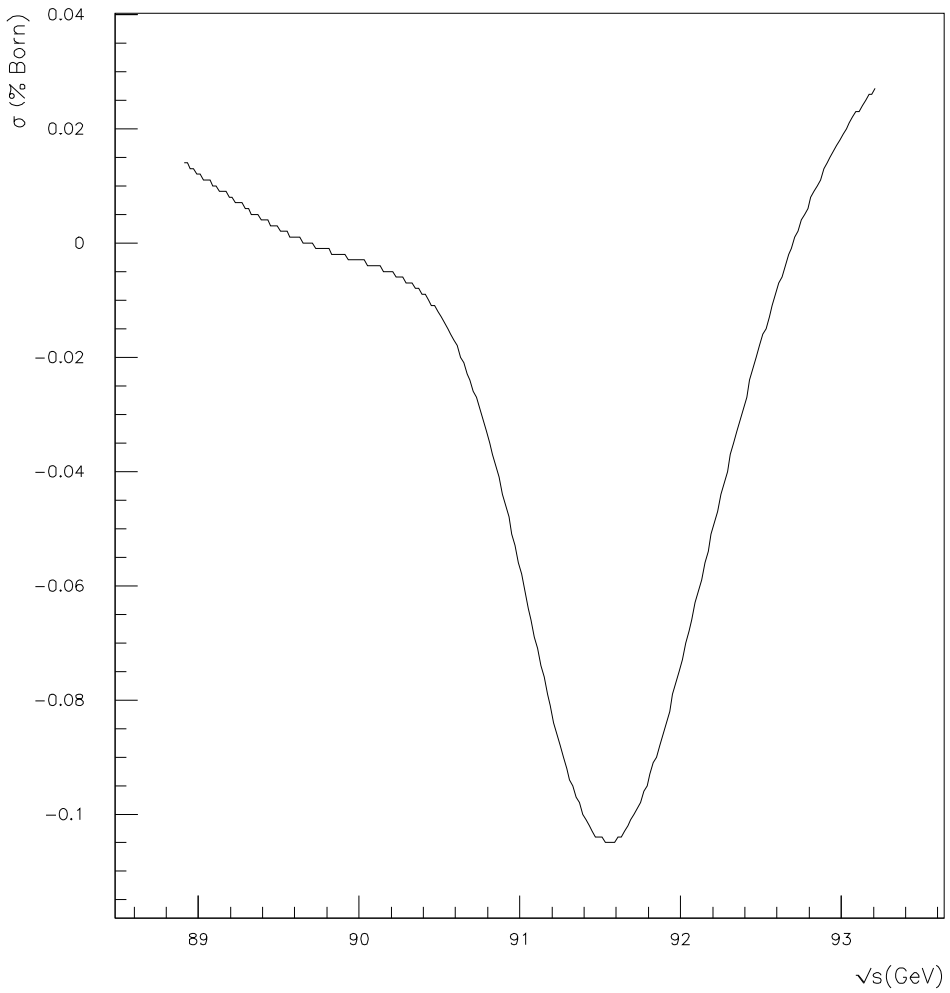

Figure 3.10: Contributions to the Born cross section from weak leading log higher-order effects for $M_Z = 91.187$, $\Gamma_Z = 2.487$ and $sin^2\theta_w = 0.2273$.

Chapter 4

Results

The SAT-detector is used to investigate weak contributions to the Bhabha QED cross section across the Z^0 resonance. I have used two methods to find these contributions to the cross section in the SAT acceptance. I have made use of the other luminosity-monitor present in DELPHI, VSAT. By using the Bhabhas collected by SAT and dividing them by the VSAT luminosity, the Bhabha cross section in the SAT acceptance is found at the 1993 energy points. This cross section is then compared to a theoretical QED cross section and the weak contributions is found. Weak effects, although not in the same acceptance, is also found by measuring the variation of the angular distribution of the cross section with respect to the centre-of-mass energy. This is done by measuring the ratio between two cross sections in the SAT-acceptance where one cross section is defined in the angular region from an angle θ_{split} to the upper limit of the SAT-acceptance and the other in the angular region from the angle θ_{split} to the lower limit of the SAT-acceptance. This is explained further below. The two methods have both their advantages and disadvantages.

4.1 SAT/VSAT

In 1993 LEP was operative at four different centre-of-mass energies, at a prescan energy[1] at 91.3 GeV and three scan-energies of 89.4, 91.2 and 93.0 GeV. Due to the relatively large weak corrections to the SAT lowest order QED Bhabha cross sections at the two scan-energies of 89.4 and 93.0 GeV (also known as the $\pm$2GeV energies) seen from theory (Figure 3.6), we thought that it was possible to see these corrections with a reasonable uncertainty from data taken with the SAT detector. In order to do this, we decided to make use of the other luminosity-monitor present in the DELPHI-experiment, VSAT. This detector is placed at very low angles well below 1^0 and from Figure 3.6 we see that the weak corrections

[1] When LEP started to run in 1993 the beam-energy was constant, later in the year the beam-energy began to scan between the other three so-called scan energies.

at these angles are very small and can therefore be neglected, contributions similar to a pure QED cross section is assumed. By dividing the number of Bhabhas detected in the SAT by the corresponding VSAT luminosity, the SAT cross section was found at each energy point. By comparing this SAT cross section with a theoretical QED cross section, the weak corrections on the QED cross section, δ, was found,

$$\delta = \left(\frac{\sigma}{\sigma_{QED}} - 1 \right) \times 100\%. \tag{4.1}$$

There was however some problems which occured because VSAT has a big error in the absolute luminosity of about 1 %. An accurate measurement of the SAT absolute cross section is therefore impossible. However, a measurement of the SAT relative cross sections for each energy point could be done, and when these was measured, the δ in Eqn. 4.1 was found. This was done by setting the cross section at the resonance peak energy point to equal the QED cross section at this energy point. Then an expression for σ_{QED} in Eqn. 4.1 was found by the use of Eqn. 3.9 where the 1/s dependence of this cross section is stated. Thereafter δ for the other energy points was easily obtained by the use of the σ_{QED} expression and the measured cross sections at the respective energy points, in Eqn. 4.1. This however meant that the corrections at the resonance peak could not be found because this was used as a normalizing point.

The data I have used is located in so-called luminosity-files where information of the luminosity down to cassette-level[2] is stored. I have written some C-programs to go through the files to choose the usable data and correct them where necessary.

As described in the previous chapter, SAT is sensitive to the position of the interaction point (IP). This effect was taken care of by leaving out the runs where the radial displacements of the IP was greater than 0.35cm (Figure 2.6). This was however not a big problem because almost all of the IP-displacements were less than this. But the z-displacements had to be taken care of. From Eqn. 2.4 we see that there is a linear dependence of the acceptance on the z-position of the IP. This was corrected for in every run by making use of IP-position information from the central tracking of DELPHI.

The result is shown in Figure 4.1 with the corresponding numerical values in Table 4.1. From the Figure we see that some of the experimental points lie outside the theoretical values even when the uncertainty is taken into consideration. We must remember that due to the uncertainty in the absolute VSAT luminosity, the experimental points can be pushed equally $\pm 1\%$ up and down the plot. The theoretical values will however still lie outside the prescan peak point and the 89.4 GeV scan-point uncertainty.

[2]Data taken with the DELPHI detector is stored in cassettes where up to 20 cassettes are needed for a LEP fill which usually lasts from 10-14 hours. Each cassette can store up to 200 MB data.

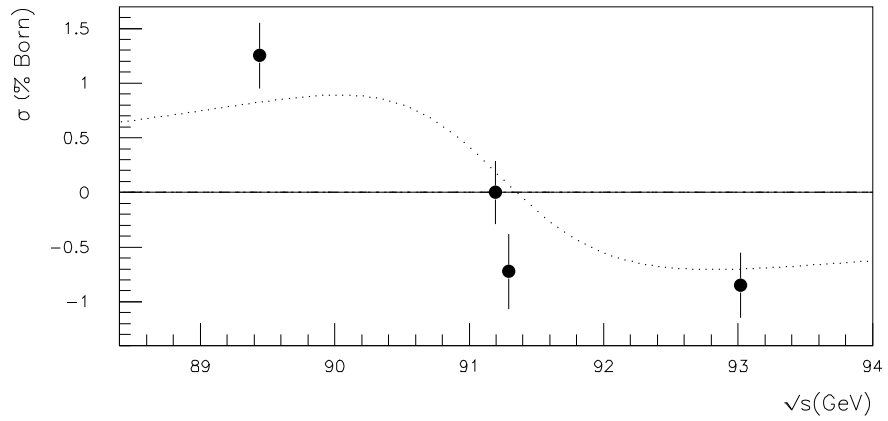

Figure 4.1: The weak contribution in % of the Born cross section at the four 1993 energies, the resonance-peak energy cross section is set equal to the QED cross section. The corresponding numerical values are presented in Table 4.1. The dotted line is the weak theoretical contribution.

Centre-of-mass Energy (GeV)	89.4	91.2	91.3	93.0
Measured Weak Contribution %	1.25	0.00	-0.72	-0.85
Statistical uncertainty %	0.30	0.29	0.34	0.30
SAT systematical uncertainty %	0.24	0.24	0.24	0.24
VSAT systematical uncertainty %	0.10	0.05	0.09	0.11
Theoretical Contribution %	0.73	0.18	0.07	-0.67

Table 4.1: The weak contribution in % of the Born cross section at the four 1993 energies, the resonance peak energy cross section is set to equal the QED cross section. The SAT and VSAT systematical uncertainty are taken from [18] and [28,13] respectively.

4.2 SAT

The other method I have used is to divide SAT into two angular bins at an angle θ_{split} and then find the ratio between Bhabhas in the two parts at each energy-point. A difference in these ratios means that there exist non-QED contributions to the cross section. This method has an advantage over the above method because we now only have to use data from one detector and therefore do not have to think about the uncertainty element the use of data from two detectors involve. The

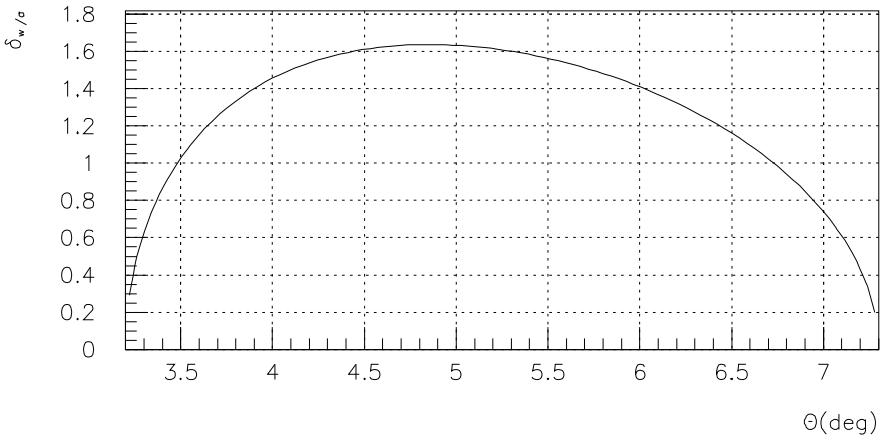

Figure 4.2: The ratio $\frac{\delta}{\sigma}$ as a function of the polar angle, θ_{split}, where the detector is split, at the +2GeV energy point.

VSAT has a strong dependence on beam parameters, and errors in connection with these dependences are eliminated. The number of Bhabhas available is however smaller and this will affect the statistical uncertainty.

4.2.1 θ_{split}

The first task I had to overcome was to find the angle where the detector should be split to get the best result. To obtain this, I used my analytical programs and the $1/\theta^3$-distribution of the differential cross section (3.8), and found $N_{s,d}$, number of standard deviations, as an approximate function of θ_{split}. $N_{s,d}$ is defined as δ/σ, where δ is defined as

$$\delta = \left(\frac{ratio}{ratio_{peak}} - 1 \right) \times 100\%, \tag{4.2}$$

where the ratios are between the cross sections in the highest and lowest angle part of the split detector, and σ is the statistical uncertainty of δ. Figure 4.2 shows how $N_{s,d}$ varies as a function of θ_{split}. The optimal θ_{split} value was then determined. From Figure 4.2 it can be seen that this value lies around 4.8 degrees. It can also be seen that δ at this angle is only $1.6\times\sigma$. The number of Bhabhas taken by the SAT at each energy point varies from about 250000 to 430000, where the largest number of Bhabhas is at the energy point at the resonance peak. With the new STIC-detector these numbers will increase due to its bigger visible cross section and then a better result can be achieved.

Throughout this chapter I will use both θ in degrees and radius in cm to describe where the detector is split. The relationship between θ and the radius,

r, is:

$$r = tan\theta \times z, \tag{4.3}$$

where z is the distance from the origin to the SAT calorimeters. This distance is 231.8 cm.

4.2.2 Cuts and results

To measure δ as a function of the centre-of-mass energy, I made use of SAT-ntuples, which are data files where the data collected by the SAT is stored in a format readable by the physics analysis program PAW [29]. The cuts which were used to choose the wanted Bhabha events, are:

1. Radius in the masked calorimeter inside the outer ring of readout elements to avoid edge effects at the calorimeter surface.

2. Radius in the unmasked calorimeter more than 2.5 cm from the inner edge to reduce background.

3. Less than half of the shower energy in the masked calorimeter in the inner ring of readout elements to avoid contamination from events passing inside the mask and entering the calorimeter through the inner surface.

4. Radius greater than 4.0 cm from the inner edge if cluster energy is greater than $1.5 \times E_{beam}$ to avoid letting low-energy photons and minimum ionizing particles which hit the readout system (fibers, light guides and photodiodes) and simulate high energy depositions, count as events.

5. Energy in both calorimeters greater than $0.65 \times E_{beam}$.

6. Azimuthal position in the masked calorimeter more than 8^0 from vertical junction between the calorimeter half-barrels to reject background caused by the tail of the showers penetrating the ϕ mask.

7. Acoplanarity angle[3] between two opposite clusters less than 20 degrees to suppress background from off momentum electrons.

More information on these cuts can be found in references [26, 27].

I summed the Bhabhas for each energy with the above cuts and with θ greater than and less than the angle where the detector was split, θ_{split}. The ratios in Eqn. 4.2 were then determined. And by dividing the $\pm$2GeV energy points by the ratio at the peak energy, the correction, δ, defined in Eqn. 4.2, was determined. I used my analytic formulae again to compare this δ to theory. Since the corrections in the

[3]Defined as the angle between a line drawn from one cluster through origo to the opposite calorimeter and the line drawn from origo to the other cluster, when these lines are projected into the X-Y plane.

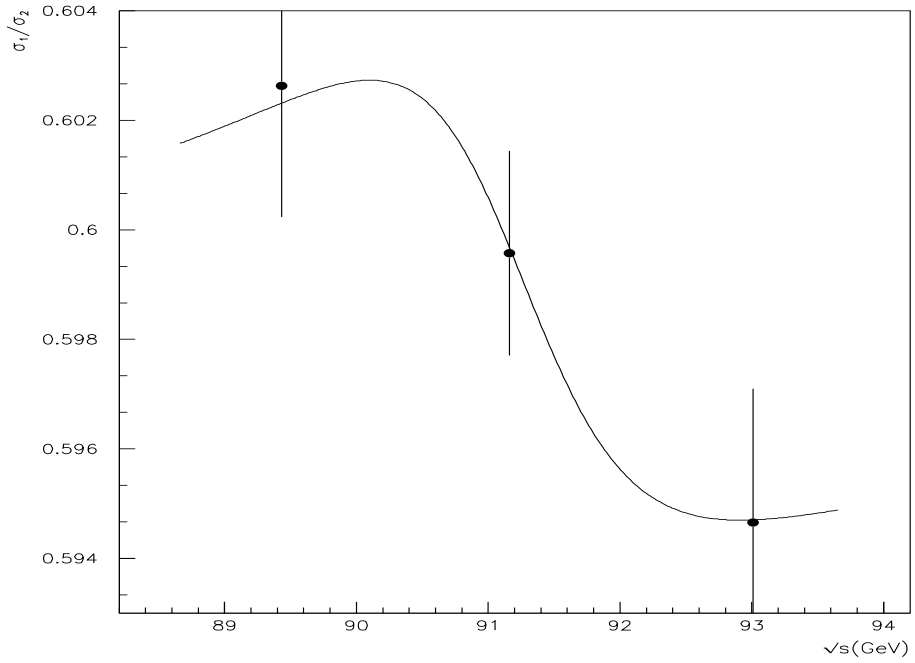

Figure 4.3: The ratio between the cross sections in the two parts of the split detector, σ_1 in the upper part and σ_2 in the lower, as a function of the CMS-energy. The full line is the theoretical ratio normalized to the experimental point at the Z^0 peak.

lowest-angle part of the split detector are non-negligible, theoretical calculations of the corrections only in the highest-angle part of the detector, as in the SAT/VSAT method, do not suffice. A calculation of the cross section in both parts had to be done. After doing this, the same ratios as above can be found and the theoretical δ for the scan-points are easily obtained. As in the SAT/VSAT method, the δ found here is not the correction to the QED cross section, but the difference between the corrections of the ± 2 GeV energy points in the scan and the corrections at the Z^0 peak, to the QED cross section.

To clarify, Figure 4.3 shows the ratio between the cross sections in the upper and lower parts of the split detector, respectively, at the different centre-of-mass energies together with the corresponding theoretical values. The theoretical ratio is normalized to the experimental point at the Z^0 peak[4]. The experimental ratios

[4]Due to uncertainties in the SAT geometry, an exact theoretical radial cut could not be set. The theoretical ratio thus had to be normalized to the experimental ratio at the Z^0 resonance peak.

	Centre-of-mass Energy (GeV)		
	89.4	91.2	93.0
Radius(cm)	Measured Weak Effects (δ)		
16.5	0.26±0.40	0.00±0.31	-0.80±0.40
17.5	0.29±0.38	0.00±0.30	-0.95±0.39
18.5	0.29±0.39	0.00±0.31	-0.85±0.40
19.0	0.36±0.40	0.00±0.31	-0.86±0.40
19.5	0.51±0.40	0.00±0.31	-0.82±0.41
20.0	0.42±0.40	0.00±0.31	-0.88 ±0.41
20.5	0.52±0.41	0.00±0.32	-0.72±0.42
21.5	0.30±0.45	0.00±0.35	-0.51±0.46
22.5	0.30±0.46	0.00±0.36	-0.57±0.48

Table 4.2: Numerical values of the plots in Figure 4.5. The errors are statistical.

are then used in (4.2) and δ is found for the two ± 2 GeV scan-points.

Figure 4.4 shows how the theoretical δ varies when the detector is split at different radii. δ is set to equal 0 at the energy of the Z^0 peak (as I did in the experimental calculation). This explains why the contributions seem much larger at the ± 2 GeV-energy point above peak-energy than below. The weak $O(\alpha)$-corrections contribute with an approximate 0.2% effect to the Born cross section at the energy point at the Z^0 peak and if δ is set to equal this value at the resonance peak energy, the contributions above and below this energy will become more alike. In Figure 4.4 it is the difference between the weak correction from 88 to 94 GeV and the correction at the Z^0 peak that is shown. The Figure shows that δ grows with larger θ_{split}, but the statistical uncertainty grows[5] too and the best result is therefore obviously not achieved at the largest possible angle (see Figure 4.2).

Figure 4.5 shows how the experimental δ varies when the detector is split at different radii. It can be seen that the uncertainty grows when the detector is split at larger radii. The figure in the middle is found from Figure 4.2 to give the best result. The corresponding numerical values are shown in Table 4.2.

The result when the detector is split at an radius of 19.5 cm is shown in Figure 4.6 together with the theoretical values. As can be seen from this figure, the experimental points agree very well with the corresponding theoretical values. The statistical uncertainty is however quite big.

[5]That is if θ_{split} is bigger than the angle where the ratio between the Bhabhas in the two detector-parts equals 1.

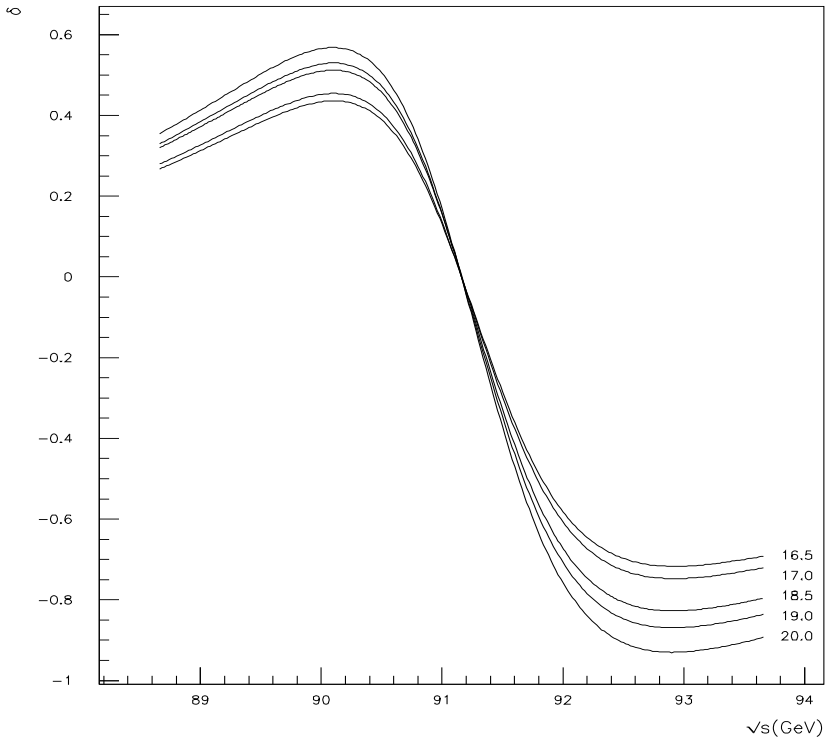

Figure 4.4: The theoretical differences in % between the ratio of the cross sections in the two parts of the split SAT detector and the ratio at the resonance peak as a function of centre-of-mass energy for five different split-radii. The numbers on the plot show at which radius (cm) the detector was split.

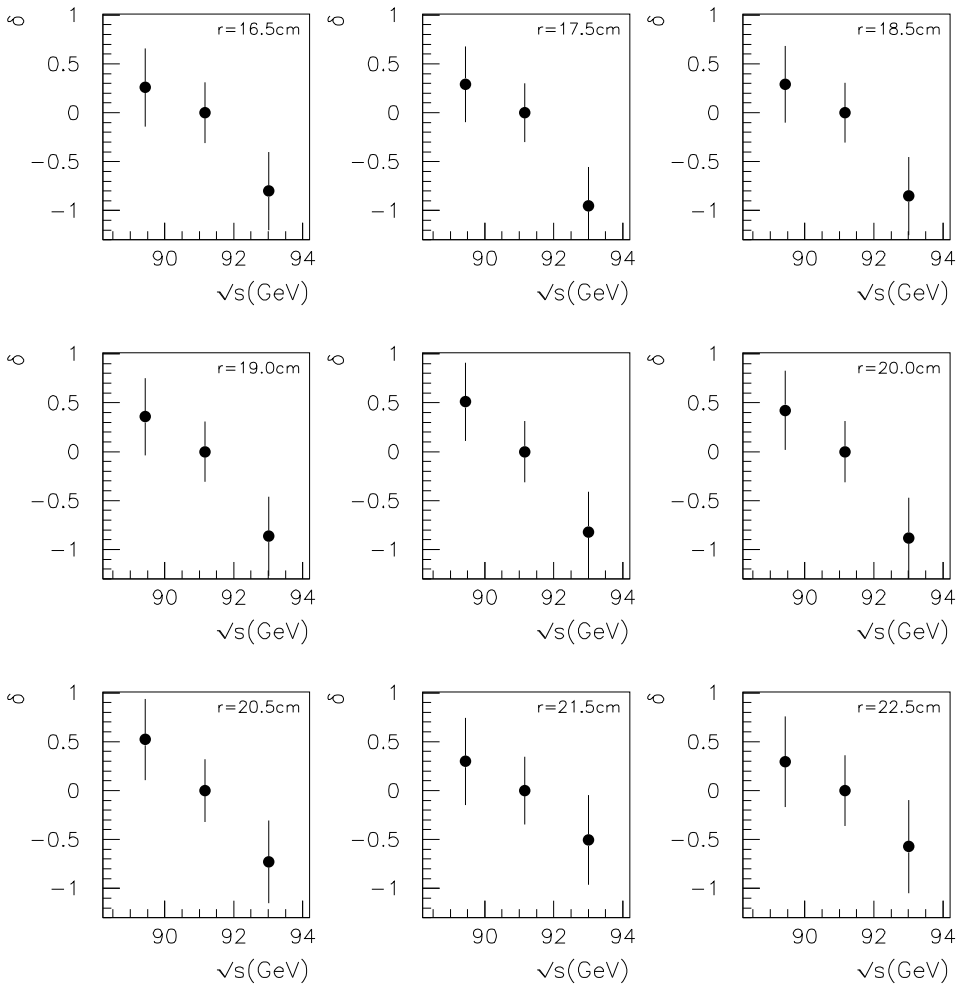

Figure 4.5: The differences between the ratio of the Bhabhas in the two parts of the split detector and the ratio at the resonance peak for the two ± 2 GeV energy-points, that is δ (defined in the text), when the detector is split at a radius r.

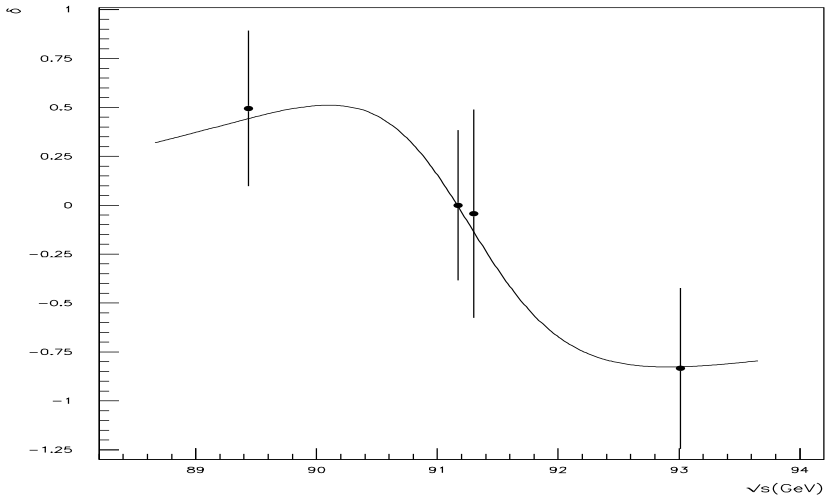

Figure 4.6: Measurement of the parameter δ, described in the text, when the detector is split at a radius r=19.5 cm. The full line is the theoretical dependence calculated with $M_Z = 91.187$, $\Gamma_Z = 2.487$ and $sin^2\theta_w = 0.2273$.

4.2.3 Other methods

The method used above is not the only method one can use to extract the weak contributions from the data taken with the SAT detector. An other, and presumably better, way to extract the weak contributions is to split the detector into more than two angular bins. This will allow for a more detailed study of the variation of the angular distribution of the cross section with respect to the centre-of-mass energy. More information can then be read from the data. This method is however not used in this thesis due to the limited amount of time available.

4.3 Fit to $sin^2\theta_W$

By making use of the function minimization and error analysis program MINUIT [30], I fitted the theoretical formulae with $sin^2\theta_W$ as a free parameter to the three experimental measured energy points. Figure 4.7 shows how the weak corrections depends on this parameter. As can be seen from the figure, the corrections grow larger with bigger $sin^2\theta_W$. The fitted value of $sin^2\theta_W$ is 0.21 ± 0.05. The error is quite big, but we can conclude that the result is in good agreement with the presently known value [5] of 0.2247 ± 0.0019.

Centre-of-mass Energy (GeV)	89.4	91.2	91.3	93.0
Measured Weak Effects(δ)	0.50	0.00	-0.04	-0.83
Statistical uncertainty	0.40	0.38	0.53	0.41
Systematical uncertainty	0.24	0.24	0.24	0.24
Theoretical δ	0.44	0.00	-0.14	-0.79

Table 4.3: Numerical values of the plots in Figure 4.6. The systematical uncertainty is taken from [18].

4.4 Effects on fits to the Z^0 mass and width

The program BABAMC was used for the theoretical calculation of the visible cross section in the luminosity measurement in DELPHI. As this program only calculates the cross section to the precision of $O(\alpha)$, it could be interesting to see how the introduction of weak higher-order contributions affects the values of the Z^0 mass and width calculated without higher order contributions.

4.4.1 The Z^0 Lineshape

The Z^0 resonance shape can be determined with very high precision in e^+e^- annihilation measurements at LEP. The collision energy in LEP has been varied over several steps across the Z^0 resonance (energy-scans) in some of the past years (1989, 1990, 1991 and 1993 with a number of 10, 7, 7 and 4 energy points, respectively each year) observing the absolute cross section for the production and subsequent decay of the Z^0 boson into well defined states. This makes it possible to determine the Z^0 mass, total decay width and peak cross section. 70% of the total decay width comes from the hadronic decay channel and most of the statistical precision therefore comes from this channel. Only about 10% of Z^0's decay to a charged lepton pair and the remaining ~20% decays into a neutrino pair and will go undetected. The separate measurements of the leptonic and hadronic lineshapes allows the determination of the corresponding partial decay widths and, thus, more rigorous tests of the Standard Model. The lineshape is sensitive to the number of light neutrino types in Nature. Each additional neutrino type will cause an decrease of the peak cross section, σ^0, by 13%, and an increase of the total decay width, Γ_Z, by 6.5%.

The shape of the cross section around the Z^0 peak can be described by a Breit-Wigner ansatz with an energy-dependent total width [31]

$$\sigma(\sqrt{s}) = \frac{12\pi\Gamma_e\Gamma_{hadrons}}{M_Z^2}\frac{s}{(s-M_Z^2)^2+s^2\Gamma_Z^2/M_Z^2}, \tag{4.4}$$

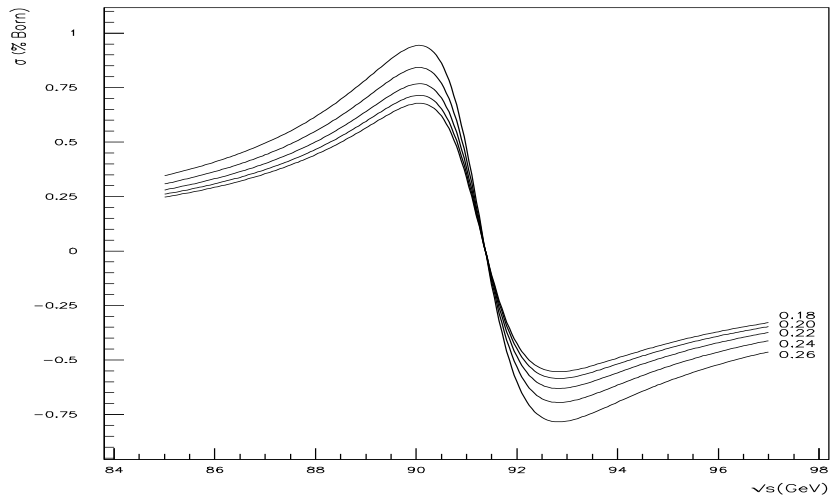

Figure 4.7: The weak corrections as a function of the centre-of-mass energy with different $sin^2\theta_W$. The numbers on the plot show the $sin^2\theta_W$ used in the calculation.

which has a maximum for

$$\sqrt{s} = \frac{M_Z}{(1+\gamma^2)^{\frac{1}{4}}}, \tag{4.5}$$

with

$$\gamma = \frac{\Gamma_Z}{M_Z}. \tag{4.6}$$

The three main properties of this distribution, that is, the position of the peak, the width of the distribution, and the height of the peak, determine respectively the values of M_Z, Γ_Z, and $\Gamma(e^+e^-) \times \Gamma(f\bar{f})$, where $\Gamma(e^+e^-)$ and $\Gamma(f\bar{f})$ are the electron and fermion partial widths of the Z^0. The quantitative determination of these parameters is done by writing analytic expressions for these cross sections in terms of the parameters and fitting the calculated cross sections to the measured ones by varying these parameters.

The LEP collaborations have chosen the following primary set of parameters for fitting: M_Z, Γ_Z, σ^0_{hadron}, $R(lepton)$, $A^{0,l}_{FB}$, where σ^0_{hadron} equals (4.4) with $s = M_Z^2$, $R(lepton) = \Gamma(hadrons)/\Gamma(leptons)$ and $A^{0,l}_{FB}$ is the forward-backward asymmetry of charged leptons. The advantage of this choice of fit-parameters is that they form the least correlated set of parameters, so that it becomes easy to combine results from the different LEP experiments [5].

The experimental determination of the Z^0 lineshape relies on cross section

Parameter	Input parameters	Fitted results	Difference (MeV)
M_Z(GeV)	91.1870	91.1866	-0.4
Γ_Z(GeV)	2.4870	2.4879	+0.9

Table 4.4: Differences between the input and fitted values of the parameters Γ_Z and M_Z.

measurements. The cross section is determined via the relation:

$$\sigma(\sqrt{s}) = \frac{N}{L}, \tag{4.7}$$

where $\sqrt{s}$ is the centre-of-mass energy where the cross section is determined, N is the number of events passing the selection criteria minus background and L is the time integrated luminosity. From the measured cross sections, the Z^0 resonance parameters are then extracted via a fit to a theoretical expression. The use of only cross section data leads to a four-parameter fit (lepton universality assumed), in other words, $A_{FB}^{0,l}$ values are not determined.

The introduction of weak higher order contributions in the determination of the visible cross section in the luminosity measurement (3.2) will change the value of L in (4.7) and therefore also the cross section. I have made use of the program ZFITTER [32], which is an analytical program for fermion pair production in e^+e^- annihilation, to calculate a hadronic cross section across the Z^0 resonance. This cross section is then perturbed with the higher order corrections calculated with the formulae in [24] with an angular acceptance from 3.2^o to 7.3^o, shown in Figure 3.10. A plot of the perturbed and unperturbed cross section is shown in Figure 4.8. MINUIT together with ZFITTER are then used to fit the hadronic cross section to the perturbed cross section points, with the parameters Γ_Z and M_Z set free. The effect due to the introduction of higher order corrections on the Z^0-mass and total decay width can then be found. The result is shown in Table 4.4 , which shows that M_Z will decrease about half a MeV and the Γ_Z will increase about 1 MeV due to the weak higher order corrections.

4.4.2 Number of light neutrino species in Nature

Three so-called "generations" of fermions (e^-, ν_e), (μ^-, ν_μ) and (τ^-, ν_τ) are known to exist and further generations with the same properties are easily incorporated within the standard electroweak theory. If any additional charged leptons exist, they must be too heavy to contribute to Z^0 decays or they would have been detected at LEP. However if additional neutrinos exist in the sequence ν_e, ν_μ,

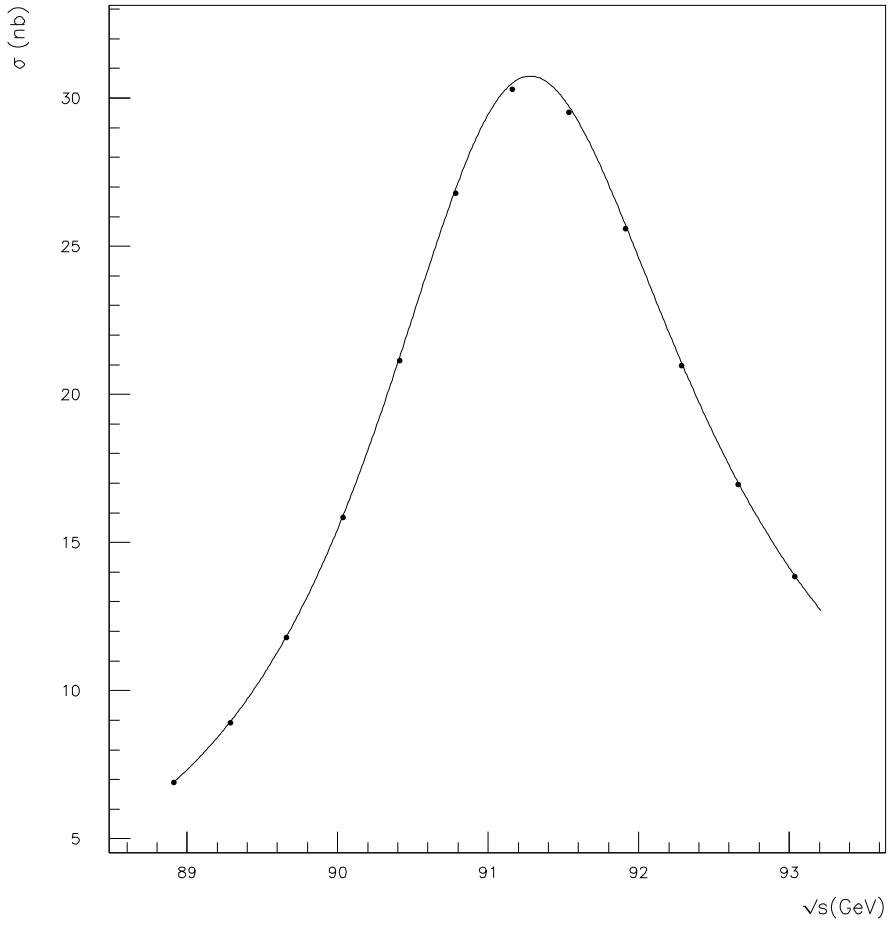

Figure 4.8: The hadronic cross section unperturbed by the weak leading higher order contributions in the luminosity measurement (full line) and the perturbed hadronic cross section (dots).

ν_τ,..., with masses much less than M_Z, then the Z^0 would decay to them with a rate given by Γ_ν which can be calculated from the standard elecroweak theory.

As mentioned above, Γ_Z is used to measure the number of light neutrino types present in Nature. A correction on Γ_Z will therefore change this number. The total Z^0 decay width can be expressed as [26]

$$\Gamma_Z = \sqrt{\frac{12\pi\Gamma_e\Gamma_{had}}{M_Z^2\sigma_{had}^0}} = \Gamma_l\sqrt{\frac{12\pi R_l}{M_Z^2\sigma_{had}^0}}, \tag{4.8}$$

where Γ_l denotes the average leptonic decay width and R_l is defined by $R_l \equiv \Gamma_{had}/\Gamma_l$. The invisible decay width, Γ_{inv}, which is defined as $\Gamma_Z - \Gamma_{had} - 3\Gamma_l$, then takes the form

$$\Gamma_{inv} = \Gamma_l\left[\sqrt{\frac{12\pi R_l}{M_Z^2\sigma_{had}^0}} - R_l - 3\right]. \tag{4.9}$$

The number of light neutrino types follows from [5]:

$$N_\nu = \frac{\Gamma_{inv}}{\Gamma_l}\left(\frac{\Gamma_l}{\Gamma_\nu}\right)_{SM}, \tag{4.10}$$

where Γ_l, Γ_ν and Γ_{inv} are the partial widths of leptons, neutrinos and the invisible Z width respectively. Using the values of the widths from [5], where the Standard Model prediction$(\Gamma_\nu/\Gamma_l)_{SM} = 1.992 \pm 0.003$, $\Gamma_l = 83.84 \pm 0.27$ and $\Gamma_{inv} = 498.2 \pm 4.2$, the number of light neutrino types is found to be 2.983 ± 0.027. A correction of $\Gamma(Z)$ by $+0.9$ MeV will increase invisible width and as a consequence the light ν type value will increase from 2.983 to 2.988. If we compare this increase of 0.005 with the total uncertainty of the present known value of ± 0.027 calculated without the higher order corrections, we see that there is a bias of 1/5 of the total uncertainty.

4.5 Summary

The SAT detector is used to measure elecroweak effects on the Bhabha cross section across the Z^0 resonance. Two methods are used. The first makes use of the VSAT detector to find the cross section in the SAT acceptance for the different energy-points. Due to the large uncertainty in the VSAT absolute luminosity, the cross section at the peak-energy is set to equal the lowest order QED cross section, and the corrections for the other energy points are then found. The result is given in Table 4.1 and Figure 4.1.

The other method makes use of only the SAT detector. The detector is split in two angular bins at an angle θ_{split}, and the ratio between Bhabhas in the two detector-parts is found at the different energy points. A difference in these ratios means that there exist an energy dependent correction to the QED cross section

which comes from weak effects. These corrections are then compared to theory. The result is given in Table 4.3 and Figure 4.6.

The theoretical formulae is then fitted to this experimental result with $sin^2\theta_W$ as a free parameter using the program MINUIT, resulting in a $sin^2\theta_W$ of 0.21 ± 0.05.

The theoretical formulae are also used to perturb a hadronic cross section as a consequence of introducing leading higher order weak corrections on the visible cross section in the luminosity measurement. By fitting a hadronic cross section to this perturbed cross section with the parameters M_Z and Γ_Z free, the effect of the introduction of these higher order corrections on the number of light neutrino types in Nature is found. The number will increase from 2.983 to 2.988, that is, by 0.17%. The total uncertainty of the number of light neutrino types in Nature is 0.91 %, which means that there exist a bias of 1/5 of the total uncertainty.

Chapter 5

Conclusions

The Standard Model of electroweak interactions has been successful in predicting a large amount of physical observables which have been measured precisely by experiments. Despite its success there are some arguments which indicates that this cannot be the final description of physics. For example, the fermion masses are unconstrained by the theory and the theory gives us no explanation of why the number of fermion families are measured to be three. Today there is a common belief that new physics will be revealed in experiments at higher energies of $\sim$1 TeV. But until accelerators which can reach these energies are built, like the LHC collider, we must continue to make tests of the Standard Model at presently available energies.

In this thesis, tests of the elecroweak theory with the SAT detector in the DELPHI experiment have been performed. This consists of 2 complementary measurements of weak contributions to the Bhabha cross section in the SAT acceptance. The relative Bhabha cross section in the SAT acceptance has been found for the different energy points in the 1993 energy-scan by using luminosity data from the VSAT detector, and the weak contributions have been extracted. Albeit the statistics could have been better, one can conclude that the result is in good agreement with the electroweak theory. Two of the points lie however a bit further away from the theoretical values than what is expected. This is believed to originate from properties of the VSAT detector which are not presently understood.

The weak contributions have also been found from splitting the SAT-detector into two angular bins and then calculating the ratio between the number of Bhabhas recorded in the two bins at each energy-point. A difference in these ratios, indicating centre-of-mass energy dependent contributions coming from weak effects, was found to agree very well with theoretical predictions from the electroweak theory. The statistical uncertainty was however too big to do precision tests of the theory. Compared to the SAT/VSAT method it is worth mentioning that, even though the uncertainty is rather big, the values of all the points agree better with the theory. This also indicates that it is properties of the VSAT de-

tector which are the reason for the small disagreement between theory and two of the points in the SAT/VSAT method.

Precision measurements of cross sections at several centre-of-mass energies around the Z^0 resonance in the DELPHI experiment (and the other experiments at LEP), which determine the Z^0 mass and width, constrain the electroweak theory so that accurate predictions of other physical observables can be made. These precision measurements depend however on an accurate luminosity measurement, which again depend on luminosity monitors with high experimental precision, high statistics and small errors in the theoretical calculation of their visible cross section.

Bhabha scattering at low angles is used to measure the luminosity in the experiments at LEP. This process is chosen due to its high cross section at low angles and its well known theory. The process is dominated by the γ t-channel at low angles but weak effects such as the Z_s-γ_t-interference can reach $\sim$1 % of the born cross section below and above the Z^0-peak energy (Figure 3.7) in the SAT acceptance. O(α) corrections to the terms containing Z-boson exchange contribute with a $\sim$0.5 % effect above the Z^0-peak energy (Figure 3.7). A higher order contribution with a maximum value of $\sim$0.1% is also present (Figure 3.10).

The SAT total theoretical error is 0.16 %. An improved theoretical calculation including weak higher order contributions was therefore needed to minimize the total theoretical error on the luminosity measurement and to avoid letting the theoretical part of the luminosity measurement unnecessarily impede the precision tests of the electroweak theory.

In this thesis various weak contributions to the Bhabha cross section has been studied. The weak LL $O(\alpha^2)$ correction to the weak $O(\alpha)$ calculation in BABAMC is presented. The effect on the lineshape measurement of introducing these $O(\alpha^2)$ corrections in the luminosity measurement, has been found to result in a small increase of the Z^0 width and small decrease of the Z^0 mass . This again has been calculated to result in a bias of 1/5 of the total uncertainty of the number of light neutrino species in Nature.

Bibliography

[1] Donald H. Perkins, *Indroduction to High Energy Physics.* Third edition, Addsion Wesley, ISBN 0-201-12105-0.

[2] G.P. Lepage, *What is Renormalization?* Newman Laboratory of Nuclear Studies, Cornell University, Ithaca, NY 14853.

[3] DELPHI Collaboration *Precision Determination of the Z^0 Resonace Parameters* DELPHI 95-62 PHYS 497, Paper submitted to the "EPS-HEP 95" Conference Brussels, 27th July-2nd August 1995.

[4] F. Halzen and A.D. Martin *QUARKS AND LEPTONS: An introductory course in modern particle physics.* Wiley. ISBN 0-471-81187-4.

[5] *Review of Particle Properties*, Physical Review **D50**, 1173 (1994).

[6] M. Mangano and T. Trippe, *The Top Quark.* Physical Review D50, 1995 off-year partial update for the 1996 edition.

[7] ALEPH Collab., D. Busculic et al., Phys. Lett. B 349 (1995) 238.

[8] DELPHI-collaboration. *The DELPHI detector at LEP.* Nucl. Inst. and Meth. **A303** (1991) 233-276.

[9] L. Bugge et al. *DELPHI SAT Luminosity Analysis: 1990.* DELPHI 91-104 PHYS-147. November 1991.

[10] L. Bugge, T. Buran, A.L. Read and E. Wilhelmsen. *The Performance of the DELPHI SAT Tracker during 1991 and its Contribution to the Absolute Luminosity Measurement.* UiO/PHYS/94-01.

[11] V. Hedberg *The new Small Angle Calorimeter in DELPHI.* DELPHI 94-148 CAL 118. November 1994.

[12] A. Benvenuti et al. *STIC, the new DELPHI luminosity monitor.* DELPHI 94-31 CAL 112. March 1994.

[13] S. Almehed et al.,*Beam parameter monitoring and interaction point measurement in DELPHI with the VSAT.* DELPHI 94-144 PHYS 453, October 1994.

[14] Almehed et al., *A silicon tungsten electromagnetic calorimeter for LEP*, NIM **A305** (1991) 320.

[15] Almehed et al., *High precision realtive luminosity measurement with a Very Small Angle Tagger (VSAT) in DELPHI*, DELPHI 92-77 PHYS 188.

[16] G. Barbiellini, B. Borgia, M. Conversi and R. Santonico. *Atti. Accad. Naz. Lincei, 44:233*, 1968.
J.F. Crawford et al., NIM 127 (1975) 173-182.

[17] A.L. Read, Private and unpublished material.

[18] DELPHI Collaboration, *Precision Determination of the Z^0 Resonance Parameters.* CERN-PPE/Paper137/Draft1, 12 January 1996.

[19] M. Caffo and E. Remiddi, *"Bhabha Scattering"*. Z PHYSICS AT LEP 1, CERN 89-08 Volume 1,eds. G. Altarelli, R. Kleiss and C. Verzegnassi, p. 171.

[20] M. Bohm, A. Denner and W. Hollik, Nucl. Phys. **B** 304 (1988) 687;
F.A. Berends, R. Kleiss and W. Hollik, Nucl. Phys. **B** 304 (1988) 712.

[21] Mogens Dam, *Bhabha Scattering Detected by a Small Angle Tagger as a luminosity Monitor for the DELPHI Experiment at LEP.* Master's thesis, Department of Physics, University of Oslo, Autumn 1987.

[22] S. Jadach et al *Higher-order radiative corrections to Bhabha scattering at low angles: YFS Monte Carlo approach.* CERN-TH.7452/94, UTHEP-94-0901 1994.

[23] S.Jadach, W.Placzek and B.F.L. Ward *Precision Calculation of the γ-Z Interference Effect in the SLC/LEP Luminosity Process.* Phys. Lett., B : 354 (1995) 349-361.

[24] W. Beenakker and B. Pietrzyk, *Contribution of terms containing Z-boson exchange to the luminosity measurements at LEP*, Physics Letters B 296 (1992) 241-250.

[25] W. Benakker, F.A. Berends and S.C. van der Marck, Nucl. Phys.**B** 349 (1991) 323; **B** 355 (1991) 281.

[26] DELPHI Collaboration, *Determination of Z^0 resonace parameters and couplings from its hadronic and leptonic decays.* Nuclear Physics **B 367** (1991) 511-574.

[27] DELPHI Collaboration, *Measurement of the Lineshape of the Z^0 and Determination of Electroweak Parameters from its Hadronic and Leptonic Decays.* CERN-PPE/94-08, 12 January 1994.

[28] L. Zanini, Torino, 1994, private communication.

[29] CERN Program Library Long Writeup Q121, *PAW, Physics Analysis Workstation.* Version 2.03 (October 1993), Application Software Group, Computing and Networks Division, CERN Geneva, Switzerland.

[30] F.James, M.Roos, *MINUIT, Function Minimization and Error Analysis*, Release 89.12j.

[31] F.A. Berends et al. *"Z Physics at LEP 1"*, CERN Report 89-08 (1989), Vol. 1,eds. G. Altarelli, R. Kleiss and C. Verzegnassi, p. 89.

[32] D. Bardin et al. *ZFITTER, An Analytical Program for Fermion Pair Production in e^+e^- Annihilation.* CERN-TH. 6442/92.

[33] F. Mandl and G. Shaw *QUANTUM FIELD THEORY, Revised Edition.* Wiley, ISBN 0-471-94186-7.

[34] M. Martinez and B. Pietrzyk *Influence of the c.m.s. energy-dependent theoretical errors on the measurement of the Z^0 parameters at LEP.* Phys. Lett., B: 324 (1994) 492-499.